UNIVERSITY OF SZEGED
FACULTY OF MEDICINE

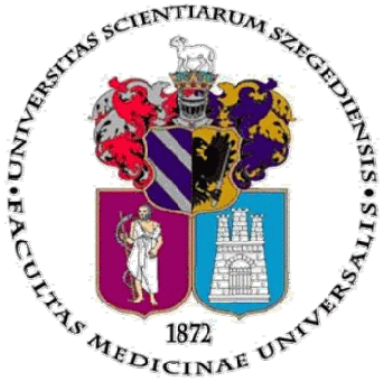

INTEGRATED OPTICAL APPLICATIONS OF BACTERIORHODOPSIN

László FÁBIÁN

PhD Thesis

Supervisor: Prof. András DÉR

INSTITUTE OF BIOPHYSICS,
BIOLOGICAL RESEARCH CENTRE OF THE HUNGARIAN ACADEMY OF SCIENCES

Szeged
2012

TABLE OF CONTENTS

1. Introduction

In 1965, director of R&D Laboratories at Fairchild Semiconductor, Gordon E. Moore has made a prediction about the future of integrated electronics, namely, about the number of electronic components that can be integrated on a silicon wafer of unit area. His first extrapolation *[Figure 1.1]* was based upon the analysis of semiconductor memory arrays and has shown that the density of components (e.g. transistors) doubles in every year [*1*]. In 1975, by taking into account the development of the somewhat less dense microprocessors, he had to modify his prediction to, that the doubling time is two years, instead of one year. The exponential growth is valid even in our days.

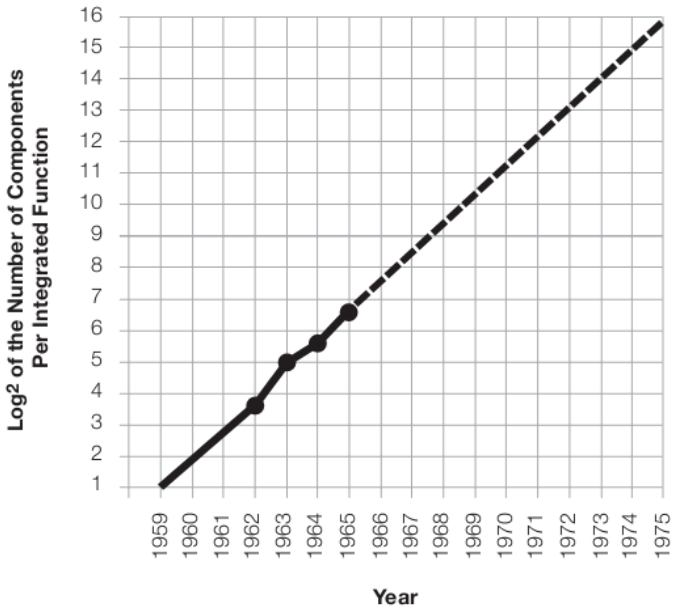

Figure 1.1: Moore's original prediction (see [1]).

However, it is often said by experts, that this exponential growth of miniaturization is not sustainable for a long time; Moore's law will soon "hit the wall". Furthermore, the growth of component density doesn't mean that the performance of integrated circuits increases correspondingly. Nowadays, integrated electronic components are fabricated by chemical, physical or electrochemical vapor deposition (CVD, PVD, ECD) methods, molecular beam epitaxy (MBE) and recently, atomic layer deposition (ALD). It is clear, that the size of

integrated electronic components can not be decreased below a limit that will be reached soon. The most important problems of today's microelectronic devices are, among others, electromagnetic interference, heat dissipation, etc.

Hence, although microelectronics will have the leading role in everyday's telecommunication and data processing applications, several alternative solutions are also intensively researched to keep up with the increasing demands of information technology.

One of the most promising approach is the field of integrated optics which provides devices operating on information signals imposed on optical wavelengths, typically in the visible and near-infrared spectrum.

1.1. Integrated Optics

Miniaturization of sensory devices, as well as coupling of optical data-processing units with microelectronics are just a few examples among the biggest challenges in integrated optics. Integrated optics *(IO)* is a rapidly emerging discipline of engineering optics aiming at integrating miniature photonic devices on a common substrate.

One of the most important areas of applications of integrated optics is telecommunication, where all-optical data processing is the most promising direction. Unlike microelectronic integration, where silicon is the dominant material, photonic integrated circuits are fabricated also from e.g. electro-optic crystals, various polymers and semiconductor materials. State-of-the-art photonic integration technology can provide the passive elements of optical integrated circuits, based either on silicon, glass or plastic materials. As the technologies are readily developed, the most challenging task of integrated optical research is to find the most suitable materials with appropriate nonlinear optical *(NLO)* properties that can serve as active elements in integrated optical circuits.

According to recent views, the versatile and cost-effective organic materials represent a promising alternative of the currently used semiconductor materials, to be the basis of active IO elements [*2*]. So far, specifically designed organic, pi-conjugated molecular materials have attracted the most interest [*3,4*], but their applicability in IO is still to be verified. Although biological materials are often disregarded in technical applications, there are several proteins

that are extremely robust, so their biological origin doesn't represent a disadvantage, on the contrary, they offer special advantages to be exploited in bioelectronic applications [*5*].

Among biological molecules under consideration for technical use, the chromoprotein bacteriorhodopsin (bR) has generated the most interest due to its extreme robustness and other physical properties [*6-8*]. In the next section, several important properties of bR will be discussed briefly.

1.2. The chromoprotein bacteriorhodopsin

Bacteriorhodopsin *(bR),* a transmembrane ion pumping protein isolated from a fraction of the outer cell membrane *(purple membrane, PM)* of the salt-loving archaebacterium *Halobacterium salinarum* [*9-13*], is the simplest known ion pump and one of the best-characterized membrane proteins.

Among other retinal-containing proteins – like halorhodopsin, sensory rhodopsin I and II [*14*] -, bR plays an important role in the energetics of the cell. Upon light absorption, bR pumps protons from the cytoplasmic side of the membrane to the extracellular space and the resulting transmembrane proton gradient is used by the ATP synthase for ATP synthesis [*15-18*]. Bacteriorhodopsin is one of the smallest ion pumping membrane proteins, therefore it serves as a model system in the investigation of the structure and functional mechanism of active ion transport processes at the atomic level.

1.2.1. Structure of bacteriorhodopsin

Bacteriorhodopsin – with a molecular weight of 26 kDa - is consisted of seven α-helices that span the purple membrane with a thickness of about 5 nm. The protein molecules are ordered in a regular two-dimensional hexagonal lattice in PM, in a trimeric form [*19-21*]. The amino acid residue sequence was also determined in one of the early studies [*22*]. The structure and function of the protein (in some details) are very similar to those of the rhodopsin found in the eye [*9*].

The atomic structure of bacteriorhodopsin *(PDB ID: 1C3W)* obtained by X-ray crystallography [*23*] is shown in *Figure 1.2*. The light-sensitive unit of the protein, a pi-conjugated chromophore (retinal), is attached to Lys-216 via a protonated Schiff's base. Several amino acid side chains which play an important role in the proton translocation process, are also indicated. The protein backbone is represented by a thin blue line. The direction of proton pumping is pointing downward from the cytoplasmic side of the membrane.

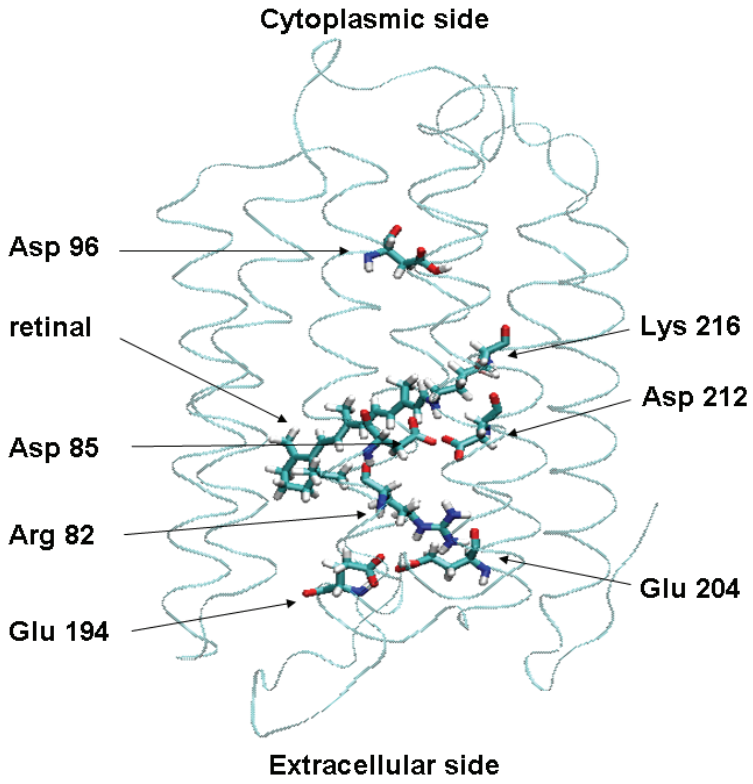

Figure 1.2: Structure of bacteriorhodopsin obtained by X-ray diffraction. The most important amino acid residues participating in the proton pumping process are also indicated.

1.2.2. The photocycle

Dark-adapted bacteriorhodopsin samples contain a mixture of *all-trans* and *13-cis* retinals, of which the latter are converted to *all-trans* under normal light conditions [*24-27*]. In the dark, the *all-trans* form is converted into the *13-cis* with a time constant of about 30 min.

The light-adapted bacteriorhodopsin molecule - in its ground state - contains an *all-trans* retinal as the light-sensing chromophore, which is covalently attached to the Lys 216 side chain via a protonated Schiff's base. Upon photon-absorption, the retinal goes to an excited state and isomerizes to its *13*-cis form *[Figure 1.3]*.

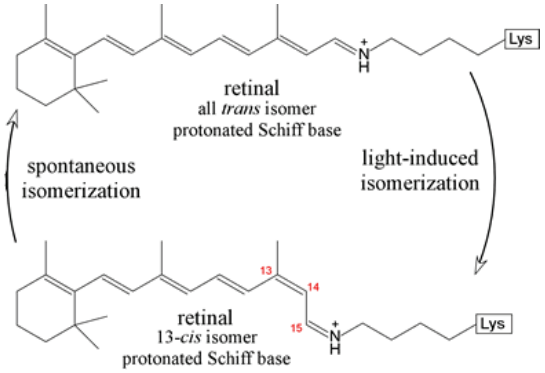

Figure 1.3: The all-trans and 13-cis isomers of the retinal.

After isomerization of the retinal, the protein undergoes a cyclic series of thermally excited conformational changes, while a proton is translocated through the membrane. In the end of the cycle, the retinal is reprotonated from the cytoplasmic side and the protein relaxes to the ground state. In the case of wild-type bacteriorhodopsin (WT bR), the characteristic life time of the whole cycle is about 10 ms. This light-induced proton transport process is called the *photocycle* [*28,29*].

During the photocycle *[Figure 1.4]*, the protein goes through several quasistable, spectrally well-distinguishable conformational states, the so called intermediate states (BR_{568}, J_{625}, K_{610}, L_{540}, M_{412}, N_{550}, O_{630}). The lower indices of the intermediate states correspond to their absorption maxima (nm).

The time course of intermediate concentrations during the photocycle can be determined by flash-photolysis experiments. After the photocycle is started by a short actinic flash, the relative population of an intermediate state can be followed by absorption spectroscopic methods in the visible range [*28*,*30-35*]. The late intermediate states are also photosensitive, the photocycle can be short-cut at any step by applying a second flash exciting the corresponding intermediate state [*36,37*].

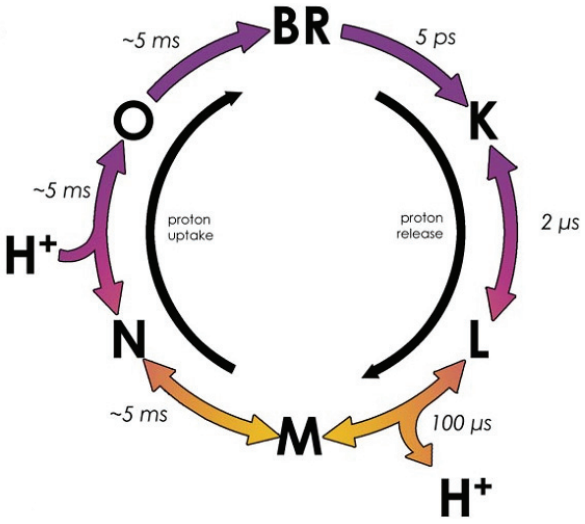

Figure 1.4: Simplified photocycle of bacteriorhodopsin [38].

Rate constants of the photocycle in solutions strongly depend on the environmental conditions, e.g. temperature, ionic strength and pH of the solution, buffers, etc. The life times of the intermediates indicated in *Fig. 1.4* correspond to room temperature and physiological conditions.

1.2.3. Refractive index changes during the photocycle

Structure and function of proteins can be studied by a lot of spectroscopic methods, ranging from X-rays to terahertz frequencies [*39-45*]. In this work, we deal only with spectroscopic properties in the visible region.

The spectra of the intermediate states were determined by several authors using different techniques. Absorption spectra used in this work *[Figure 1.5]* was measured by C. Gergely *et al.* [*46*] and were refined later by L. Zimányi [*47*].

Since we want to study the applicability of bacteriorhodopsin as an active optical material in integrated optics, one of the most important properties is the refractive index change. The absorption difference between two intermediate states also implies a corresponding refractive index change, according to the Kramers-Kronig relations.

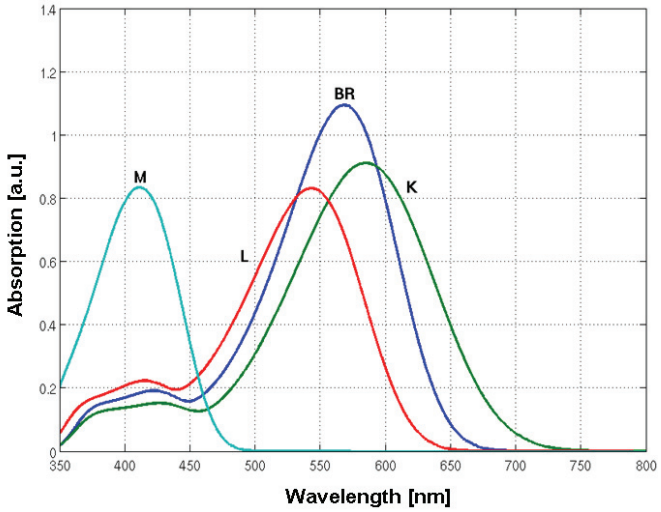

Figure 1.5: Absorption spectra of intermediate states BR, K, L and M [47].

We define the complex refractive index as:

$$n' = n + i\kappa ,$$

where n is the real refractive index, $\kappa(\omega)$ is the *extinction coefficient* which is related to the *absorption coefficient*, $\alpha(\omega)$, of the material as:

$$\alpha(\omega) = \frac{2\omega}{c}\kappa(\omega) = \frac{4\pi}{\lambda}\kappa(\omega).$$

In this notation, one of the Kramers-Kronig relations states that the real refractive index of the material is completely determined by the extinction coefficient for all frequencies [*48*,*49*]:

$$n(\omega) - 1 = \frac{c}{\pi} P \int_0^{\infty} \frac{\kappa(\omega')}{\omega'^2 - \omega^2} d\omega'$$

The letter *"P"* in front of the integral means the principal value. The refractive index changes of the intermediate states with respect to the ground state (BR) have been calculated according to the above Kramers-Kronig relation and are shown in *Figure 1.6*.

As it is expected from the absorption shift, the calculated largest refractive index change is between the BR and M states, approximately -4×10^{-3} at the wavelength of the He-Ne laser (632.8 nm). At the same wavelength, refractive index changes between the BR→K and BR→L transitions are almost equal, approx. -2×10^{-3}. The calculated refractive index

changes are comparable, or even higher than those of organic or inorganic crystals used as active materials in integrated optical devices.

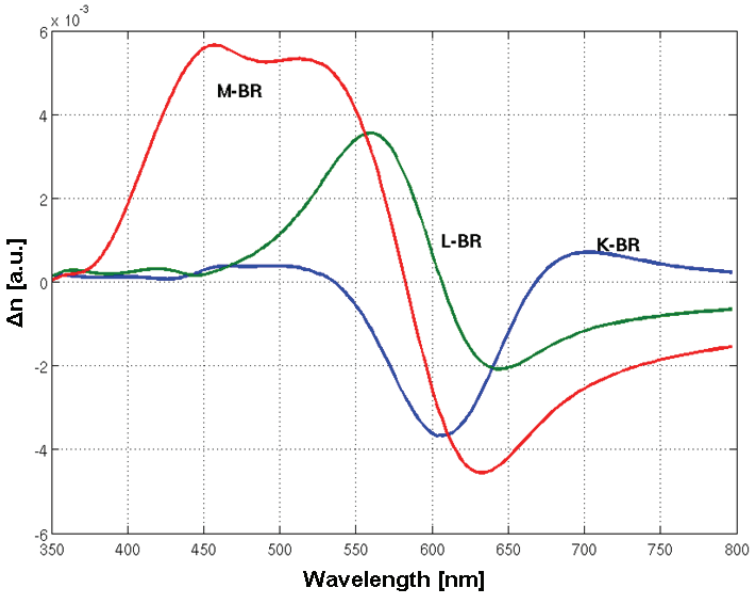

Figure 1.6: Calculated refractive index changes between the intermediate states.

2. Aim of this work

In this work, possible applications of bacteriorhodopsin containing purple membrane films as active optical material in waveguide-based integrated optical devices are under investigation. The light-induced refractive index change of bacteriorhodopsin during the photocycle is studied on different time-scales. Our aim was to demonstrate the suitability of bacteriorhodopsin as a nonlinear optical material for all-optical switching and modulation.

First, for a better understanding, derivation of some fundamental properties of the guided modes propagating in a slab optical waveguide will be given. The results and consequences of the theory, especially the concept of the effective refractive index will be used to interpret the experimental findings.

Next, in the experimental section, the following phenomena will be investigated in detail:

a) waveguide-based integrated optical switching on the *μs* time-scale using the photoreactions of the BR and M intermediate states,

b) interferometric optical switch in the *ns* regime using an integrated Mach-Zehnder interferometer, based on the refractive index change between the BR and K states, and finally,

c) waveguide-based *ps* amplitude and frequency switching based on the ultrafast BR→K transition of bacteriorhodopsin.

3. Guided waves

Generally speaking, guided waves can be electromagnetic waves of any frequency or frequency-range, whose propagation is confined in a more or less well defined region of space. Waveguides are designed (or can be even natural) structures that confine the electromagnetic waves and it is the frequency of the radiation that determines the size and the materials to be used to construct the appropriate waveguide structure. For example, waveguides for microwave frequencies (cm range) are metallic structures with size of several centimeters, while optical waveguides are dielectric structures of nano- and micrometer size. However, the common property of all electromagnetic waves is that they obey the fundamental equations of electromagnetism, namely, Maxwell's equations.

This chapter deals with the detailed analysis of guided waves propagating in an optical waveguide. While the problem can be treated using the laws and equations of ray optics (e.g. Snell's law, Fresnel equations, etc.), here we give a more rigorous solution using Maxwell's equations. First, the mode equations governing the propagation of a monochromatic plane wave in the waveguide will be derived.

3.1. The slab optical waveguide

In this part we will solve Maxwell's equations for the electric ($\vec{\mathbf{E}}$) and magnetic ($\vec{\mathbf{H}}$) fields with the appropriate boundary conditions imposed by the geometry of our model *[Fig. 3.1]*.

The slab optical waveguide consists of a (usually) glass *substrate*, a thin dielectric layer *(guiding layer, core* or *film)* made of high refractive index material and a so-called *cladding* or *adlayer* with refractive indices n_S, n_F and n_A, respectively. The substrate and the adlayer is assumed to extend infinitely in the $-x$ and $+x$ directions, while the thickness of the guiding layer is given by d. The *y*-*z* plane of our coordinate system is the bisector of the guiding layer. Throughout the theoretical analysis we assume that the wave vector of the light lies in the *x*-*z* plane and the direction of propagation inside the guiding layer is $+z$.

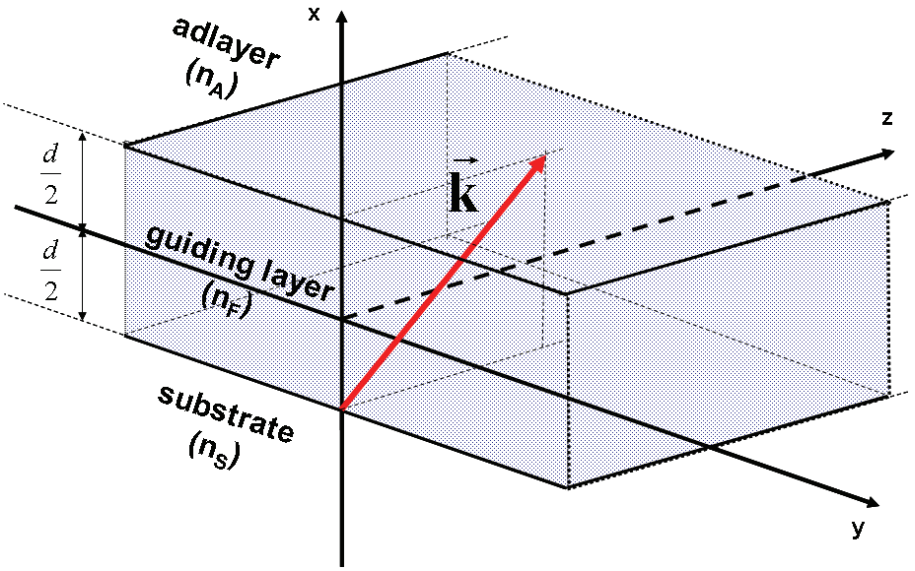

Figure 3.1: Schematic model of the slab waveguide with the wave vector ($\vec{k}$) of the propagating light, indicated by the red arrow.

We assume that all the materials consisting the waveguide are linear, isotropic, lossless and nonmagnetic ($\mu = 1$) without free charges and currents. In this case, Maxwell's equations take the following form:

$$\vec{\nabla} \cdot \vec{\mathbf{E}} = 0 \tag{1a}$$

$$\mu_0 \left(\vec{\nabla} \cdot \vec{\mathbf{H}} \right) = 0 \tag{1b}$$

$$\vec{\nabla} \times \vec{\mathbf{E}} = -\mu_0 \frac{\partial \vec{\mathbf{H}}}{\partial t} \tag{1c}$$

$$\vec{\nabla} \times \vec{\mathbf{H}} = \varepsilon_0 \varepsilon \frac{\partial \vec{\mathbf{E}}}{\partial t} \tag{1d}$$

By taking the *curl* of (1c) and (1d), and applying

$$c^2 = \frac{1}{\mu_0 \varepsilon_0}, \text{ and } \varepsilon = n^2$$

together with the well-known vector analysis identity for an arbitrary vector $\vec{\mathbf{A}}$:

$$\vec{\nabla} \times \left(\vec{\nabla} \times \vec{\mathbf{A}} \right) = \vec{\nabla} \left(\nabla \cdot \vec{\mathbf{A}} \right) - \nabla^2 \vec{\mathbf{A}}$$

we get the *wave equations* for the electric and magnetic fields inside the medium with refractive index of *n*:

$$\nabla^2\vec{\mathbf{E}} - \frac{n^2}{c^2}\frac{\partial^2\vec{\mathbf{E}}}{\partial t^2} = 0 \tag{2a}$$

$$\nabla^2\vec{\mathbf{H}} - \frac{n^2}{c^2}\frac{\partial^2\vec{\mathbf{H}}}{\partial t^2} = 0 \tag{2b}$$

We are looking for a solution in the form of a plane wave propagating along the *z* axis. Now we introduce our next assumption. Since the media are isotropic, the variation of the electric field should be independent of the *y* variable and this restriction is expressed by the spatial operator $\frac{\partial}{\partial y} = 0$,when applied to the $\vec{\mathbf{E}}$ and $\vec{\mathbf{H}}$ vectors. Therefore, the electric and magnetic fields of a monochromatic wave with an angular frequency of ω which obey the above restrictions can be written in the form:

$$\vec{\mathbf{E}}(\vec{\mathbf{r}},t) = \vec{\mathbf{E}}_0(x)\exp\left[-i(\omega t - \beta z)\right] \tag{3a}$$

$$\vec{\mathbf{H}}(\vec{\mathbf{r}},t) = \vec{\mathbf{H}}_0(x)\exp\left[-i(\omega t - \beta z)\right] \tag{3b}$$

where β is the component of the wave vector parallel to the *z*-axis, the so-called *propagation constant*. In the following, the $\vec{\mathbf{E}}_0(x)$ electric and the $\vec{\mathbf{H}}_0(x)$ magnetic field distributions across the cross-section of the waveguide will be determined.

For our trial solution of (3a), the vector Laplacian in (2a) reduces to:

$$\nabla^2\vec{\mathbf{E}} = \left(\frac{\partial^2}{\partial x^2} - \beta^2\right)\vec{\mathbf{E}},$$

while the second derivative respect to time becomes

$$\frac{\partial^2\vec{\mathbf{E}}}{\partial t^2} = -\omega^2\vec{\mathbf{E}}.$$

The same expressions hold also for the $\vec{\mathbf{H}}$ magnetic field. Substitution of these operators into the original wave equations gives the one dimensional *Helmholtz-equations* corresponding to the cross-sectional field distributions:

$$\frac{\partial^2\vec{\mathbf{E}}_0}{\partial x^2} + \gamma^2\vec{\mathbf{E}}_0 = 0 \tag{4a}$$

$$\frac{\partial^2 \vec{\mathbf{H}}_\mathbf{0}}{\partial x^2} + \gamma^2 \vec{\mathbf{H}}_\mathbf{0} = 0 \qquad \text{(4b)}$$

where the parameter γ with the *effective refractive index of the mode (N)* is introduced through

$$\gamma_i^2 = \frac{n_i^2 \omega^2}{c^2} - \beta^2 = \frac{\omega^2}{c^2}\left[n_i^2 - \frac{c^2}{\omega^2}\beta^2 \right] = k_0^2 \left(n_i^2 - N^2 \right) \qquad (5)$$

Depending on the sign of γ_i^2, solutions of (4a) and (4b) are linear combinations of exponential functions of either complex or real arguments. In a slab optical waveguide there are three kinds of propagation modes of which characteristics depend on the sign of (5) *[Table 3.1]*. The *S*, *F* and *A* indices correspond to the substrate, guiding layer and adlayer, respectively.

Substrate mode	**Guided mode**	**Radiation (air) mode**
$\gamma_S^2 > 0$	$\gamma_S^2 < 0$	$\gamma_S^2 > 0$
$\gamma_F^2 > 0$	$\gamma_F^2 > 0$	$\gamma_F^2 > 0$
$\gamma_A^2 < 0$	$\gamma_A^2 < 0$	$\gamma_A^2 > 0$

Table 3.1: Waveguide modes corresponding to different signs of γ^2 in each medium.

In the range of $\min\left(n_A, n_S\right) < N < \max\left(n_A, n_S\right)$ total internal reflection occurs at the guiding-layer – adlayer boundary, propagation modes of this kind are called *substrate modes [Fig. 3.2a]*. The $N < \min\left(n_A, n_S\right)$ case corresponds to the so-called *radiation*, or *air* modes, where no total internal reflection occurs at any of the interfaces. In this case, solutions of (4a) and (4b) are sinusoidal functions in all three layers *[Fig. 3.2b]*. From the detailed analysis of the mode equations it comes that there are infinitely large number of solutions for substrate and air modes in the valid regions of *N* mentioned above.

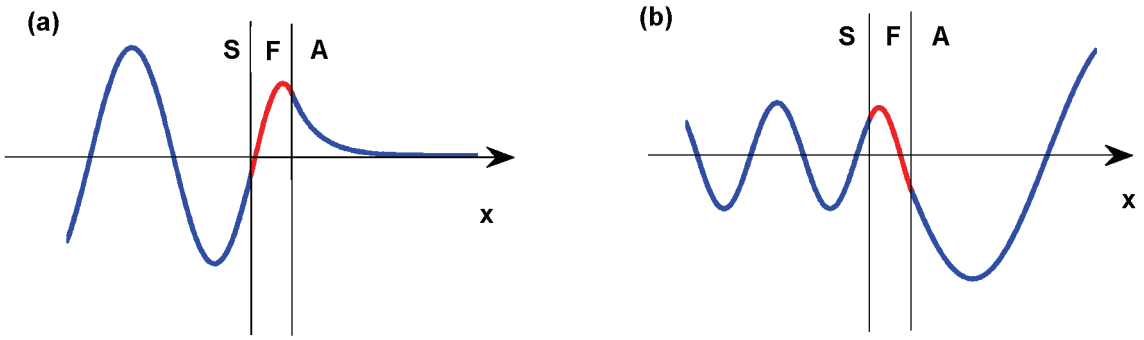

Figure 3.2: Calculated cross-sectional electric field distributions a) for a TE substrate mode with $N = 1.3$ *and b) for a TE air mode with* $N = 0.7$ *. Waveguide parameters used in the calculation are* $n_S = 1.52, n_F = 1.77, n_A = 1, d = 200\,nm, \lambda = 632.8\,nm$.

From the point of view of applications, the most interesting property of an optical waveguide is that under certain conditions the propagating light is confined in the guiding layer. Phenomenologically it can be described by consecutive total internal reflections at the substrate – film and film – adlayer interfaces. Here we present a more accurate derivation of the propagation of guided modes using Maxwell's equations. As it was mentioned before, guided modes can be excited when $\max\left(n_A, n_S\right) < N < n_F$. In this case the spatial variation of the electric field is sinusoidal in the guiding layer and vanishes exponentially in the substrate and adlayer. In the following, we will discuss separately the propagation properties of transversal electric (TE, s-polarized) and transversal magnetic (TM, p-polarized) modes. The differential equation system corresponding to the field distributions will be solved together with the boundary conditions which state that the components of the $\vec{\mathbf{E}}$ electric and $\vec{\mathbf{H}}$ magnetic fields parallel to the interface of two adjacent media with different refractive indices must be continuous on the boundary.

3.1.1. The TE guided mode

In the transversal electric (TE) guided mode the electric field has only one non-zero component, that is, parallel to the *y-axis*, which can be written as $\vec{\mathbf{E}}_0 = \left[0, E_y\left(x\right), 0\right]$. We

require the electric field inside the adlayer and substrate to vanish as $x \to \pm\infty$, respectively. The harmonic behavior of the electric field profile inside the guiding layer is described by a sinusoidal function containing an indefinite phase constant. The differential equation system describing the *y*-component of the electric field that fulfill these conditions in the three layers is:

$$E_{y,S} = A\exp\left[\gamma_S\left(x+\frac{d}{2}\right)\right], \qquad \text{if } x<-\frac{d}{2} \tag{6a}$$

$$E_{y,F} = B\sin\left(\gamma_F\left(x+\frac{d}{2}\right)+\varphi\right), \qquad \text{if } -\frac{d}{2}\le x\le\frac{d}{2} \tag{6b}$$

$$E_{y,A} = C\exp\left[-\gamma_A\left(x-\frac{d}{2}\right)\right], \qquad \text{if } \frac{d}{2}<x \tag{6c}$$

The magnetic field from (1c) is:

$$\vec{\mathbf{H}}(\vec{\mathbf{r}},t) = \frac{-i}{\omega\mu_0}\left(\vec{\nabla}\times\vec{\mathbf{E}}(\vec{\mathbf{r}},t)\right)$$

In the case of a TE polarized wave, $\vec{\mathbf{H}}_\mathbf{0}$ has non-zero components only in the *x* and *z* directions, and we can write it as $\vec{\mathbf{H}}_\mathbf{0} = \left[H_x(x), 0, H_z(x)\right]$, where

$$H_x = \frac{\beta}{\omega\mu_0}E_y, \qquad H_y = 0, \qquad H_z = -\frac{i}{\omega\mu_0}\frac{\partial E_y}{\partial x}$$

The tangential components of the magnetic field in the different layers are:

$$H_{z,S} = -\frac{i}{\omega\mu_0}A\gamma_S\exp\left[\gamma_S\left(x+\frac{d}{2}\right)\right], \qquad \text{if } x<-\frac{d}{2} \tag{7a}$$

$$H_{z,F} = -\frac{i}{\omega\mu_0}B\gamma_F\cos\left(\gamma_F\left(x+\frac{d}{2}\right)+\varphi\right), \qquad \text{if } -\frac{d}{2}\le x\le\frac{d}{2} \tag{7b}$$

$$H_{z,A} = \frac{i}{\omega\mu_0}C\gamma_A\exp\left[-\gamma_A\left(x-\frac{d}{2}\right)\right], \qquad \text{if } \frac{d}{2}<x \tag{7c}$$

Our aim is to determine the effective mode indices *(N)* of the allowed modes in a slab waveguide with given parameters. The tangential components of the electric and magnetic fields – namely E_y and H_z – must be continuous at the interface of two media. Equating the

corresponding fields at $x=-\frac{d}{2}$ and $x=\frac{d}{2}$ yields a system of equations from which we can get:

$$\tan\varphi=\frac{\gamma_F}{\gamma_S} \qquad \text{and} \qquad \tan\left(\gamma_F d+\varphi\right)=-\frac{\gamma_F}{\gamma_A}$$

Using the trigonometric identity

$$\tan\left(\alpha+\beta\right)=\frac{\tan\alpha+\tan\beta}{1-\tan\alpha\tan\beta}$$

and introducing

$$\tan\Phi_{S,E}=\frac{\gamma_S}{\gamma_F} \qquad \text{and} \qquad \tan\Phi_{A,E}=\frac{\gamma_A}{\gamma_F}$$

we arrive to the TE *mode equation*:

$$\gamma_F d=\Phi_{S,E}+\Phi_{A,E}+m\pi \tag{8a}$$

or

$$k_0 d\sqrt{n_F^2-N^2}=\arctan\sqrt{\frac{N^2-n_S^2}{n_F^2-N^2}}+\arctan\sqrt{\frac{N^2-n_A^2}{n_F^2-N^2}}+m\pi \tag{8b}$$

Here the *m* parameter comes from the periodicity of the *tan* function and is called the *mode number*. Instead of the continuous effective index spectrum of the substrate and air modes, (8a) or (8b) have only one solution for each *m*. The left and right hand sides of the mode equation for different mode numbers are plotted on *Figure 3.3*.

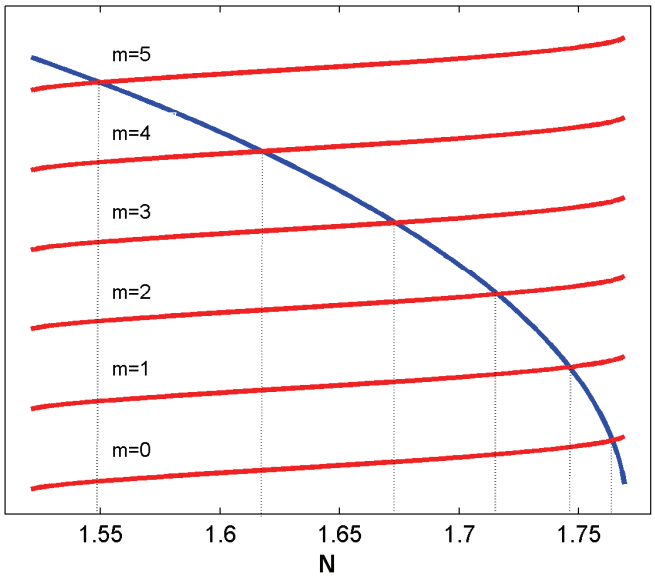

Figure 3.3: Left (blue) and right (red) hand side of the TE mode equation for different mode numbers. Waveguide parameters used in the calculation are $n_S = 1.52, n_F = 1.77, n_A = 1, d = 2\,\mu m, \lambda = 632.8\,nm$.

3.1.2. The TM guided mode

In the TM (or p-polarized) guided mode the electric field oscillates in the plane parallel to the plane of incidence, in our case, the *x*-*z* plane. In this case, instead of the electric field, we write the polarization vector of the magnetic field in the form of $\vec{\mathbf{H}}_0 = \left[0, H_y(x), 0\right]$ and the corresponding vector for the electric field will be derived from Maxwell's equations.

We get similar relations for the *y*-component of the magnetic field as for the electric field in the previous case:

$$H_{y,S} = A\exp\left[\gamma_S\left(x+\frac{d}{2}\right)\right], \qquad \text{if } x < -\frac{d}{2} \tag{9a}$$

$$H_{y,F} = B\sin\left(\gamma_F\left(x+\frac{d}{2}\right)+\varphi\right), \qquad \text{if } -\frac{d}{2} \le x \le \frac{d}{2} \tag{9b}$$

$$H_{y,A} = C\exp\left[-\gamma_A\left(x-\frac{d}{2}\right)\right], \qquad \text{if } \frac{d}{2} < x \tag{9c}$$

The electric field from (1d) is:

$$\vec{\mathbf{E}}(\vec{\mathbf{r}},t)=\frac{i}{\varepsilon_0\omega n^2}\left(\vec{\nabla}\times\vec{\mathbf{H}}(\vec{\mathbf{r}},t)\right).$$

Since $\vec{\mathbf{H}}$ has only a non-zero component in the *y*-direction, $\vec{\mathbf{E}}$ will have non-zero components in the *x* and *z*-directions, and can be written as:

$$E_x=\frac{\beta}{\varepsilon_0\omega n^2}H_y, \qquad E_y=0, \qquad E_z=\frac{i}{\varepsilon_0\omega n^2}\frac{\partial H_y}{\partial x}$$

Therefore, the tangential component (E_z) in the different layers is:

$$E_{z,S}=\frac{i}{\varepsilon_0\omega n_S^2}A\gamma_S\exp\left[\gamma_S\left(x+\frac{d}{2}\right)\right], \qquad \text{if } x<-\frac{d}{2} \tag{10a}$$

$$E_{z,F}=\frac{i}{\varepsilon_0\omega n_F^2}B\gamma_F\cos\left(\gamma_F\left(x+\frac{d}{2}\right)+\varphi\right), \qquad \text{if } -\frac{d}{2}\le x\le\frac{d}{2} \tag{10b}$$

$$E_{z,A}=-\frac{i}{\varepsilon_0\omega n_A^2}C\gamma_A\exp\left[-\gamma_A\left(x-\frac{d}{2}\right)\right], \qquad \text{if } \frac{d}{2}<x \tag{10c}$$

Again, applying the boundary conditions for the electric and magnetic fields at $x=-\frac{d}{2}$ and $x=\frac{d}{2}$, we get a system of equations for the effective refractive index and the unknown phase term:

$$\tan\varphi=\frac{n_S^2}{n_F^2}\frac{\gamma_F}{\gamma_S} \qquad \text{and} \qquad \tan\left(\gamma_F d+\varphi\right)=-\frac{n_A^2}{n_F^2}\frac{\gamma_F}{\gamma_A}$$

Introducing

$$\tan\Phi_{S,M}=\frac{n_F^2}{n_S^2}\frac{\gamma_S}{\gamma_F} \qquad \text{and} \qquad \tan\Phi_{A,M}=\frac{n_F^2}{n_A^2}\frac{\gamma_A}{\gamma_F},$$

we arrive to the TM mode equation:

$$\gamma_F d=\Phi_{S,M}+\Phi_{A,M}+m\pi \tag{11a}$$

or

$$k_0 d\sqrt{n_F^2-N^2}=\arctan\left[\frac{n_F^2}{n_S^2}\sqrt{\frac{N^2-n_S^2}{n_F^2-N^2}}\right]+\arctan\left[\frac{n_F^2}{n_A^2}\sqrt{\frac{N^2-n_A^2}{n_F^2-N^2}}\right]+m\pi \tag{11b}$$

In *Figure 3.4*, the effective indices of the first three TE and TM guided modes are plotted as a function of the guiding layer thickness. For example, in a 300 nm thick slab waveguide with the parameters indicated, only the zeroth TE and TM modes can propagate, therefore it is called a *single-mode* waveguide at $\lambda = 632.8\,nm$. For a given guiding layer thickness, the effective indices of the modes are decreasing with increasing mode number.

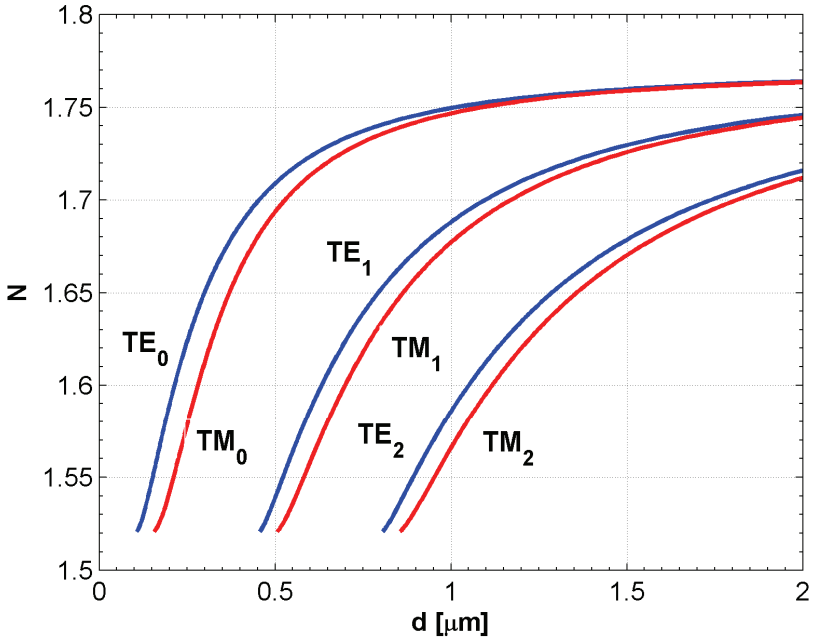

Figure 3.4: Effective indices of several modes as function of the guiding layer thickness. Waveguide parameters: $n_S = 1.52, n_F = 1.77, n_A = 1, \lambda = 632.8\,nm$.

As it is one of the measurable quantities in waveguide based applications, it is important to know how the effective index of a guided mode changes when the refractive index of the adlayer changes. In *Figure 3.5*, the effective indices of TE_0 and TM_0 modes are shown for two different adlayer refractive indices. Two experimentally important properties can be deduced from the *Figs. 3.4* and *3.5*, namely, that *a)* for a given guiding layer thickness the TM_m mode has always lower effective index than that of the corresponding TE_m mode and *b)* the effective index of a certain mode increases with increasing adlayer refractive index.

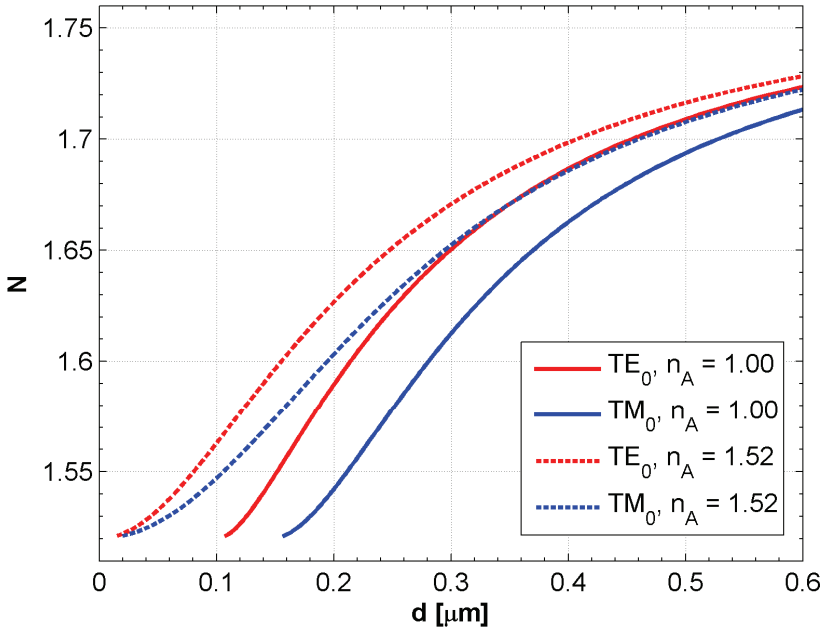

Figure 3.5: Effective indices of the TE_0 and TM_0 modes as function of the guiding layer thickness in the cases of different adlayer refractive indices.

Waveguide parameters: $n_S = 1.52, n_F = 1.77, n_A = 1.00$ *and* $1.52, \lambda = 632.8\,nm$.

An important property of the waveguide is the so-called *cutoff-frequency* or *cutoff-wavelength* that determines the minimum frequency (maximum wavelength) of the radiation that can be guided in a given structure. For an electromagnetic radiation of wavelength above this threshold there is no solution of the mode equations, the conditions required for the guided mode to exist can not be fulfilled. The cutoff condition occurs when one of the phase changes upon total reflection becomes zero. Since usually $n_A < n_S$, this is the case, when $N = n_S$. For the zeroth *TE* and *TM* modes the cutoff-wavelengths are defined by:

$$\lambda_{c,TE} = 2\pi d \frac{\sqrt{n_F^2 - n_S^2}}{arctg\sqrt{\frac{n_S^2 - n_A^2}{n_F^2 - n_S^2}}}, \qquad \text{and} \qquad \lambda_{c,TM} = 2\pi d \frac{\sqrt{n_F^2 - n_S^2}}{arctg\left[\frac{n_F^2}{n_A^2}\sqrt{\frac{n_S^2 - n_A^2}{n_F^2 - n_S^2}}\right]}$$

The cutoff-wavelengths as a function of the adlayer refractive index are shown in *Figure 3.6*.

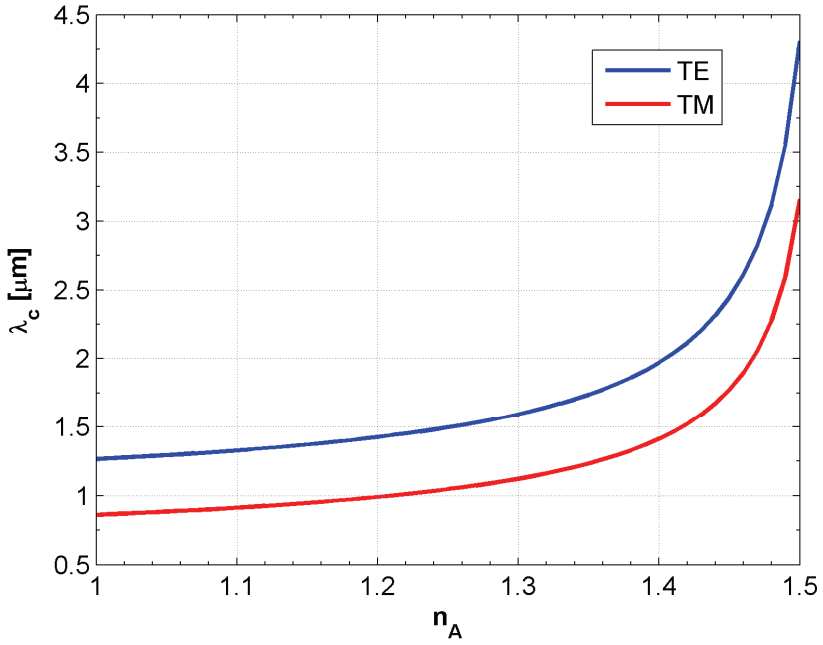

Figure 3.6: The cutoff-wavelength for the zeroth TE and TM modes.
Waveguide parameters: $n_S = 1.52, n_F = 1.77, n_A = 1.0, d = 200\ nm$.

The *cutoff thickness* of the waveguide can be defined similarly: this is the minimum thickness of the guiding layer in which a guided mode can propagate *[Figure 3.7]*. For a particular wavelength the cutoff thickness of the *m*th TE and TM modes are:

$$d_{c,TE} = \frac{\lambda_0}{2\pi} \frac{\arctan\sqrt{\frac{n_S^2 - n_A^2}{n_F^2 - n_S^2}} + m\pi}{\sqrt{n_F^2 - n_S^2}}, \qquad \text{and} \qquad d_{c,TM} = \frac{\lambda_0}{2\pi} \frac{\arctan\left[\frac{n_F^2}{n_A^2}\sqrt{\frac{n_S^2 - n_A^2}{n_F^2 - n_S^2}}\right] + m\pi}{\sqrt{n_F^2 - n_S^2}}$$

The $\Phi_{S,i}$ and $\Phi_{A,i}$ $(i = E, M)$ phases changes come from the Goos – Hänchen shifts for the two differently polarized modes that occur at the substrate-film and film-adlayer interfaces, respectively. These phase shifts reflect the *evanescent* property of the propagating wave. Upon total internal reflection the wave slightly penetrates into the medium with lower refractive index as it was reflected from a virtual interface displaced from the real one. The characteristic distance, measured from the interface, where the magnitude of the evanescent field decays to its *1/e* value is called the *penetration depth*.

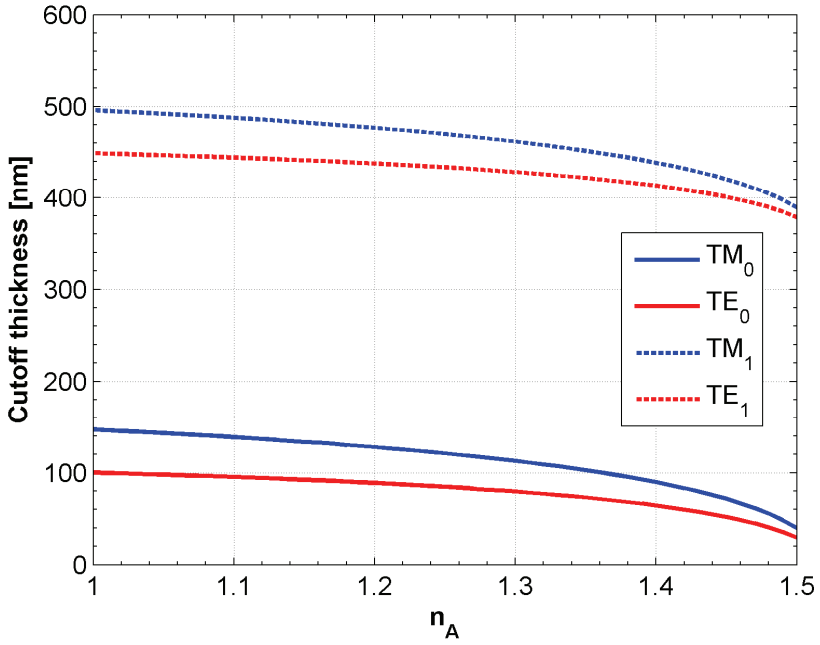

Figure 3.7: The cutoff thickness as function of adlayer refractive index.

Waveguide parameters: $n_S = 1.52$, $n_F = 1.77$, $\lambda = 632.8\ nm$.

The magnitude of the penetration depth in medium *i (i=A,S; for adlayer and substrate, respectively)* is in the order of wavelength and is given by:

$$\Delta x_i = \frac{\lambda_0}{2\pi} \frac{1}{\sqrt{N^2 - n_i^2}} \frac{1}{\left[\frac{N^2}{n_F^2} + \frac{N^2}{n_i^2} - 1 \right]^{\rho}}$$

with $\rho = 0, 1$ for TE and TM modes, respectively. The penetration depths for the two polarization and two different adlayer refractive indices are shown in *Figure 3.8* as a function of the effective index. Penetration depth also affects the validity of equations derived for the three-layer waveguide. In the calculations above, we assumed that the adlayer occupies the semi-infinite space above the guiding layer. If the penetration depth is higher than the adlayer thickness, equations corresponding to three layers are no longer valid, one have to use those derived for a four-layer waveguide [*50*].

For both polarizations, the penetration depth increases with increasing adlayer refractive index; this result is also supported by the fact that in waveguide structures light tends to propagate towards the regions of higher refractive index. Also, we have seen in *Figure 3.3*,

that modes of lower mode number have higher effective index. Since these modes propagate under high incident angles and are more confined in the guiding layer, penetration into the cladding is smaller. For higher order modes, which propagate under small incident angles, the momentum is higher in the direction perpendicular to the propagation, therefore they are "pushed" out into the cladding in a greater extent upon total internal reflection.

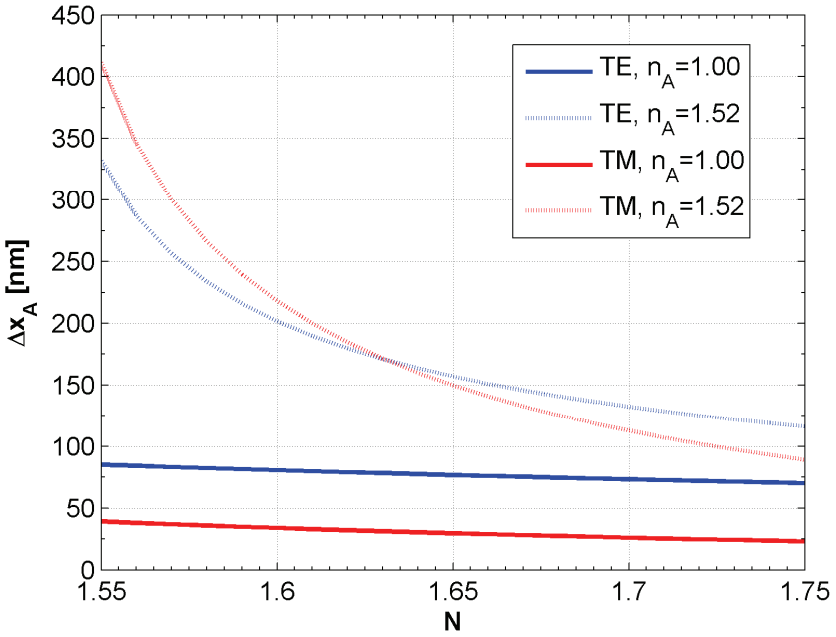

Figure 3.8: Penetration depth of the evanescent field.
Waveguide parameters: $n_S = 1.52, n_F = 1.77, n_A = 1.0,$ *and* $1.52, \lambda = 632.8\ nm$.

The sum of the waveguide thickness and the two penetration depths,

$$d_{eff} = d + \Delta x_S + \Delta x_A$$

is called the *effective waveguide thickness*, the cross section within the significant amount of the mode power is propagating. It can be shown that if P is the total power propagating across the cross section defined by the effective thickness, the fractional part of the power in medium i (i=S,A for substrate and adlayer, respectively) can be written as:

$$\frac{P_i}{P} = \frac{n_F^2 - N^2}{n_F^2 - n_i^2} \frac{\Delta x_i}{d_{eff}}$$

In the derivation above we have shown how the most important properties of a monochromatic, electromagnetic plane wave propagating in a three-layer slab optical

waveguide can be calculated. However, these parameters (e.g. propagation constant, effective index, penetration depth, etc.) are all microscopic or can not be measured directly. Even so, a lot of experimental methods exist that use the benefits of guided waves. One of them, that we will investigate in the next section, is the Optical Waveguide Lightmode Spectroscopy (OWLS). From now on, the electromagnetic wave under consideration (if not mentioned otherwise) is taken to be a monochromatic laser beam in the visible wavelength range.

3.2. Optical Waveguide Lightmode Spectroscopy (OWLS)

In practical measurements, the above calculated parameters have to be connected to macroscopically observable ones. Single mode waveguides operating at visible and near-infrared (NIR) wavelengths typically have a core diameter comparable to the wavelength.

The first problem one encounters is the coupling of light into the guiding layer. Using Snell's law, it can be easily shown that it is impossible to excite a guided mode in the core just by directing the beam at a certain angle into the core through the substrate (or adlayer) *[see Figure 3.9]*.

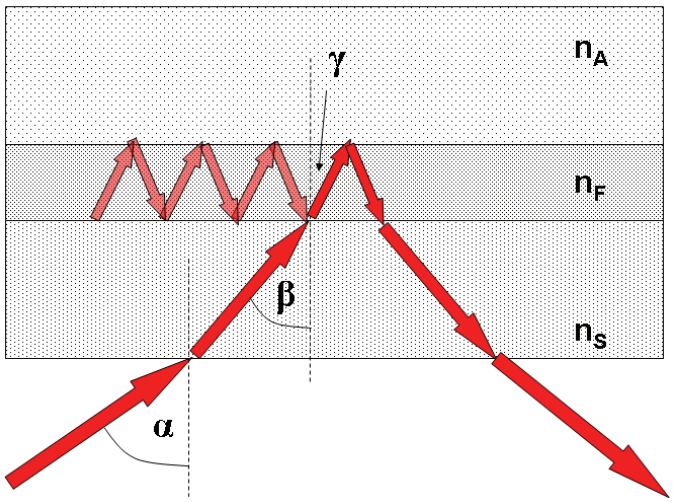

Figure 3.9: Schematic path of an incident laser beam through the substrate.

To prove this, let us assume that the incoupling is possible, so that a laser beam impinging the substrate under a proper angle will become a guided mode and remains in the core, propagating along a zigzag path. Consequently, it would mean - since the direction of

propagation is reversible - that an originally guided wave propagating in the core region can leave the waveguide without any reason, which is, of course, impossible. Therefore, our original assumption was wrong, the beam can not be coupled into the guiding layer in such a way. Even if the incidence angle α at the air-substrate interface is chosen so that angle γ at the core-adlayer boundary is higher than the critical angle, after one total reflection the beam will be scattered out of the waveguide.

3.2.1. Incoupling methods

There exist several methods by which a laser beam can effectively be coupled into a waveguide. In this section only those, namely, end coupling and grating coupling will be discussed, that were used in our experiments.

3.2.1.1. End excitation

Guided modes can be directly excited by illumination from the polished end of the core. In all cases, the numerical aperture *(NA)* of the incident beam must be matched by that of the waveguide. Only the infinitesimal rays inside the *acceptance angle* (red and orange) of the waveguide will remain in the core, the rest (black) are scattered out *[Figure 3.10]*.

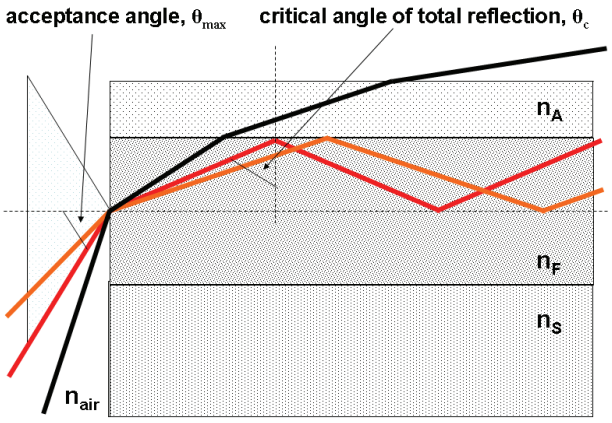

Figure 3.10: Schematics of end coupling.

Now, imagine a light ray coming from the air and impinging the polished end of the core at an angle of $\vartheta_{\max}$ (acceptance angle) and propagating under the critical angle of total reflection, ϑ_c (the red ray in *Fig. 3.10*). From Snell's law we get:

$$n_{air} \sin \vartheta_{\max} = n_F \cos \vartheta_c$$

Taking its square:

$$\frac{n_{air}^2}{n_F^2} \sin^2 \vartheta_{\max} = 1 - \sin^2 \vartheta_c = 1 - \frac{n_A^2}{n_F^2}$$

$$NA = n_{air} \sin \vartheta_{\max} = \sqrt{n_F^2 - n_A^2}$$

This is the numerical aperture of the waveguide. Since the condition of total reflection must be satisfied both at the substrate-core and core-adlayer interfaces, a more precise expression of the above formula is:

$$NA = n_{air} \sin \vartheta_{\max} = \sqrt{n_F^2 - \left(\max\left(n_A, n_S\right)\right)^2}$$

Effective coupling of a laser beam to a multi-mode waveguide by end excitation can be achieved with perfect matching between the numerical apertures of the focusing lens and the waveguide. All modes that have finite overlap integral with the incident field will be excited. If the NA of the incident beam is less than that of the waveguide, higher modes will not be excited, while in the opposite case a fraction of the incident beam is lost.

In the case of single-mode waveguides, the polarization and the transversal intensity distribution of the laser beam also have to be matched with that of the waveguide mode to be excited. For example, if a focused laser beam is used to excite the TM_0 mode, the phase front must be flat and the spot size must be matched with the mode size. Also, an asymmetric waveguide mode (e.g. TE_1) won't be excited by an incoming field symmetric with respect to the center of the waveguide.

In practical applications, since the core thickness of a single-mode optical waveguide is usually less than 1 μm, end coupling requires precise positioning and alignment of the laser beam or the optical fiber used for incoupling. Similarly, when an optical fiber is used to collect the guided beam at the end of the core, the NA of the fiber has to be matched to that of the waveguide.

3.2.1.2. The grating coupler

Another type of the widely used dispersive optical elements to couple light into a waveguide is the grating coupler. In contrast to the prism coupler, which can be regarded as an "external" coupling device, the grating coupler is an internal one, which means that it is embedded and fixed in the waveguide itself. Fabrication of the grating can be done by several methods, for example, by sol-gel technique - where a master grating is used to make the replicas – an amplitude grating can be fabricated, or by ion implantation techniques, by which the refractive index of a certain region of the waveguide is modulated, resulting in a phase grating.

In the analysis of the grating coupler, first we give a short review on the working principles of optical gratings. Let us investigate an optical grating with period of Λ and a monochromatic plane wave of wavelength λ incident on the grating under angle α *[Figure 3.11a]*.

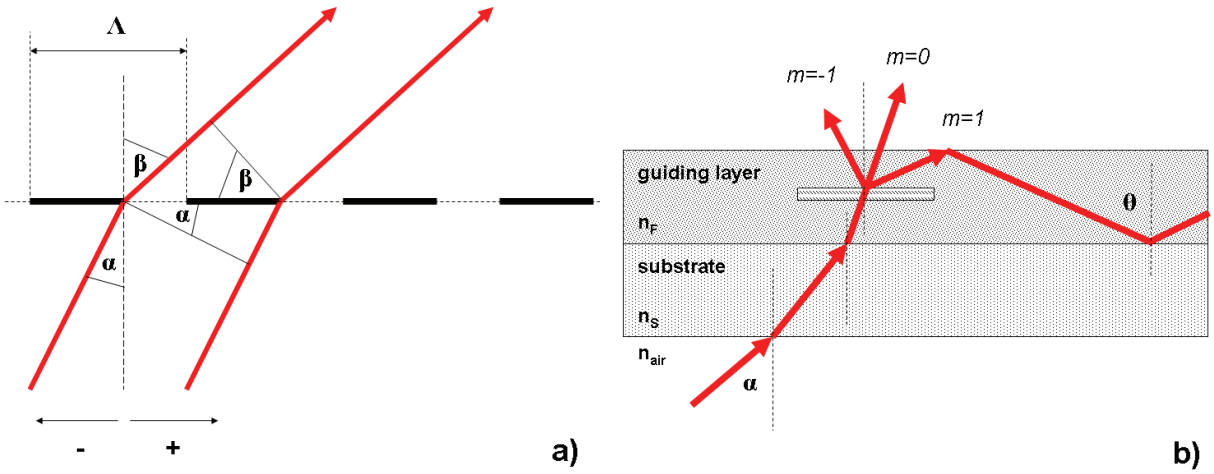

Figure 3.11: Schematic working principle of a) the optical grating and b) the grating coupler.

We assume that an angle is negative when it is measured to the left from the normal of the surface and positive otherwise. In this case, according to the *grating equation*, for the β_m direction of the *m*th order diffracted beam:

$$\sin\beta_m = m\frac{\lambda}{\Lambda} - \sin\alpha_m$$

Now, let's see, what happens when a grating is embedded inside the guiding layer. Following the path of a beam incident on the substrate, diffracted by the grating and finally, confined in the guiding layer as a guided mode, we can evaluate the relationship between the angle of incidence and the effective index of this mode *[Figure 3.11b]*:

$$n_F \sin \vartheta = m \frac{\lambda_0}{\Lambda} - n_{air} \sin \alpha$$

Taking into account that the wave vector of a guided mode in the direction of propagation is

$$\beta = k_0 N = k_0 n_F \sin \vartheta ,$$

we arrive to the desired relation between the incident angle of the beam and the effective mode index:

$$N = m \frac{\lambda_0}{\Lambda} - n_{air} \sin \alpha$$

In practice, the refractive index of air is taken to be $n_{air} = 1.00$ and only the diffracted beam of first order is used.

As some of the essential incoupling methods used in our experiments have been summarized, now we present the most basic experimental arrangement of the OWLS technique.

3.2.2. OWLS in experiments

The basic principle of Optical Waveguide Lightmode Spectroscopy is the measurement of the effective index of a certain guided mode and the change of the guided power upon external perturbation. Since, to the first order approximation, the effective refractive index is a function of several parameters of the waveguide,

$$N = N\left(n_S, n_F, n_A, d, \lambda_0\right)$$

accurate measurement of N allows us to calculate these parameters. For example, during the calibration procedure, one measures N_{TM} and N_{TE}. Usually, the substrate is made of glass, therefore, n_S is a known parameter. If the waveguide doesn't have an additional cladding, the adlayer is the medium in which the measurement is done, e.g. air or a liquid of known refractive index. In this way, we have the two mode equations for the TE and TM modes, and

two unknown parameters, namely, the thickness and refractive index of the guiding layer. Substituting the measured effective indices into the corresponding mode equations, the unknown parameters of the waveguide can be calculated numerically.

The methodology of an OWLS measurement is the following. The waveguide is fixed on a rotational stage by which the angle of incidence can be varied with high precision *[Figure 3.12]*. A grating coupler is used to couple the incident light into the waveguide. The output intensity of the guided wave is measured by two photodiodes or photomultipliers, which are attached to the ends of the waveguide, either directly or through optical fibers. The detected intensity signal is usually acquired by a computer or digital oscilloscope.

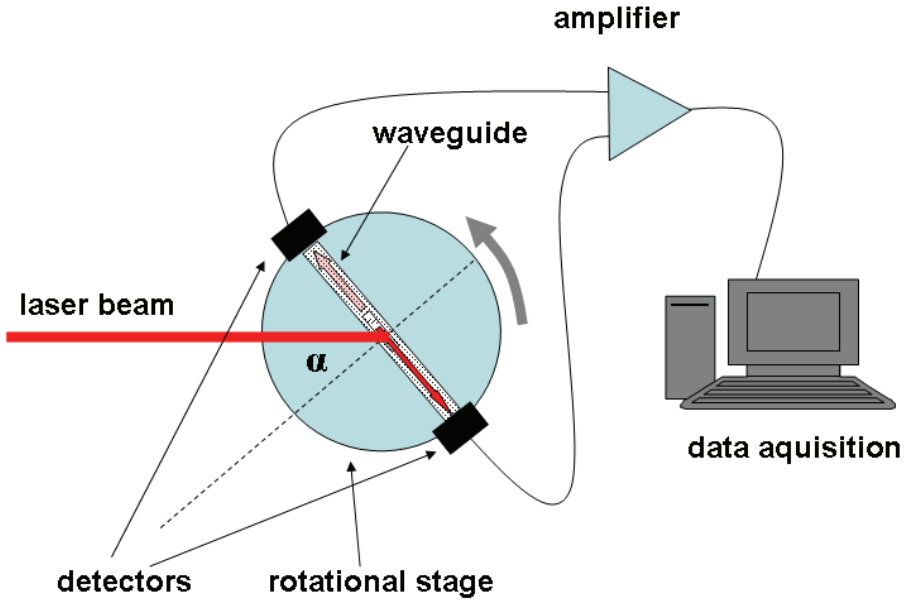

Figure 3.12: Experimental setup of a typical OWLS measurement.

At particular angles of incidence angles sharp intensity peaks can be observed at the output, indicating that a guided wave is propagating along the waveguide. Since the mode equations give a well defined effective index value for the TM and TE guided modes, the detected signals should be a Dirac-delta function. However, if we assume that the illuminated length of the grating along the direction z is L_z, then, according to the optical uncertainty principle, the inequality

$$L_z \delta k_z = L_z k_0 \delta N \cong 2\pi$$

determines the minimum spread of the effective refractive index of the mode. Introducing a so called detuning variable

$$\bar{N} = N - \frac{\lambda}{\Lambda} + \sin\alpha$$

the uncertainty of the effective mode index as function of this variable becomes

$$\delta\bar{N} = \delta N = \frac{\delta k_z}{k_0} = \frac{\lambda}{L_z},$$

which means that instead of a Dirac-delta, a sharp incoupling peak of finite width centered at the exact value of the effective index can be observed *[Figure 3.13]*. The width of the grating used in our experiments is about 1 mm, so if the beam of a He-Ne laser emitting at 632.8 nm is coupled into the waveguide, the corresponding minimum width of the incoupling peak is about 6×10^{-4}. Practically, due to the non-zero divergence of the beam and imperfections in the grating, the width of the incoupling peak is much wider, typically in the order of several hundredths of a degree.

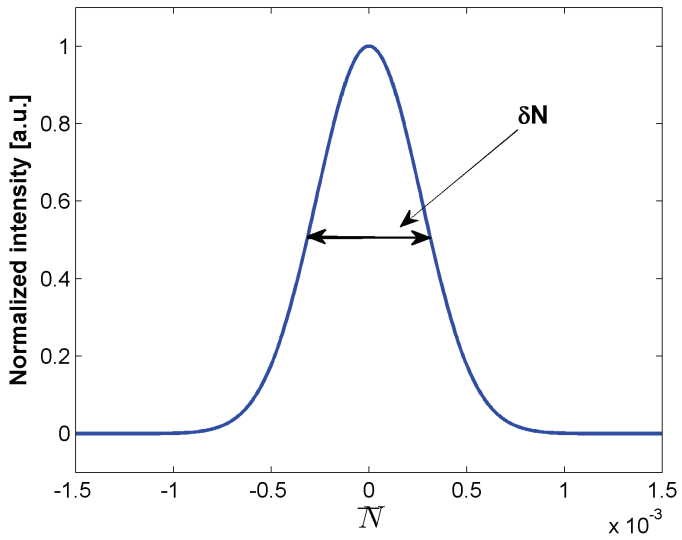

Figure 3.13: The incoupled intensity as a function of detuning.

In the calibration stage, the polarization plane of the laser is rotated so that the incident beam on the waveguide consists of both TE and TM polarized light. The angle of incidence is slowly varied between $-\alpha_{\text{lim}}$ and α_{lim}, in the interval where the effective refractive index is smaller than n_F. Here

$$\alpha_{\text{lim}} = \arcsin\left|\frac{\lambda}{\Lambda} - n_F\right|.$$

In a single-mode waveguide there are four peaks, two of them correspond to the zeroth TM and TE modes propagating in the $+z$, and the other two correspond to those propagating in the $-z$ direction, detected by the detectors at the ends of the waveguide *[Figure 3.14]*. The relative ratio of the TE and TM peaks depends on the polarization angle of the incident beam.

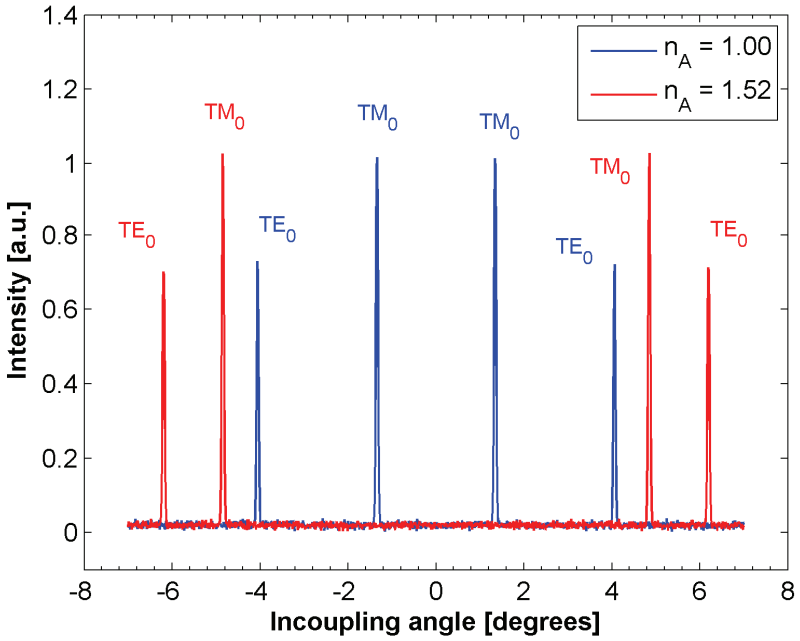

Figure 3.14: The zeroth order TM and TE guided modes measured by the OWLS technique. Waveguide parameters: $n_S = 1.52$, $n_F = 1.77$, $n_A = 1.0$, *and* 1.52, $\lambda = 632.8\ nm$, $d = 200\ nm$.

Since the guided modes are symmetric to the normal incidence, measurement of the incoupling angles in both the negative and positive directions allows us to determine the position of the zero angle. From the positions of the incoupling peaks in the case of air adlayer, the thickness and refractive index of the guiding layer can be calculated by solving the mode equations. Then, if an additional layer of a material is coated on the top of the guiding layer, the refractive index of this adlayer can already be calculated using the calibrated parameters.

We must note that the above derived equations for the three-layer waveguide are valid only in such cases, when the cladding is much thicker than the corresponding penetration depth of the guided mode under investigation.

OWLS is widely used in sensory applications. Any external perturbation that involves the change of the adlayer refractive index – e.g. photo-induced changes, specific binding, adsorption, etc. - can be detected or monitored by this technique [*51-56*]. In sensory applications a very important property is sensitivity, which is the measure of the change in the effective index of a guided mode as a function of the change of adlayer refractive index. The sensitivity of the zeroth TM and TE modes can be written as:

$$\frac{\partial N}{\partial n_A} = \frac{n_A}{N}\frac{n_F^2 - N^2}{n_F^2 - n_A^2}\frac{\Delta x_A}{d_{eff}}\left[2\frac{N^2}{n_A^2} - 1\right]^{\rho},$$

where $\rho = 0,1$ corresponds to the TE and TM modes, respectively. The sensitivity plots of the zeroth TM and TE modes as a function of guiding layer thickness are shown in *Figure 3.15* in the case of three different adlayer refractive indices. As the refractive index of the adlayer increases, the cutoff thickness decreases and the penetration depth increases as well. There is a well defined thickness for each adlayer refractive index, at which the sensitivity reaches its maximum. For increasing adlayer refractive index the corresponding optimum of the guiding layer thickness decreases.

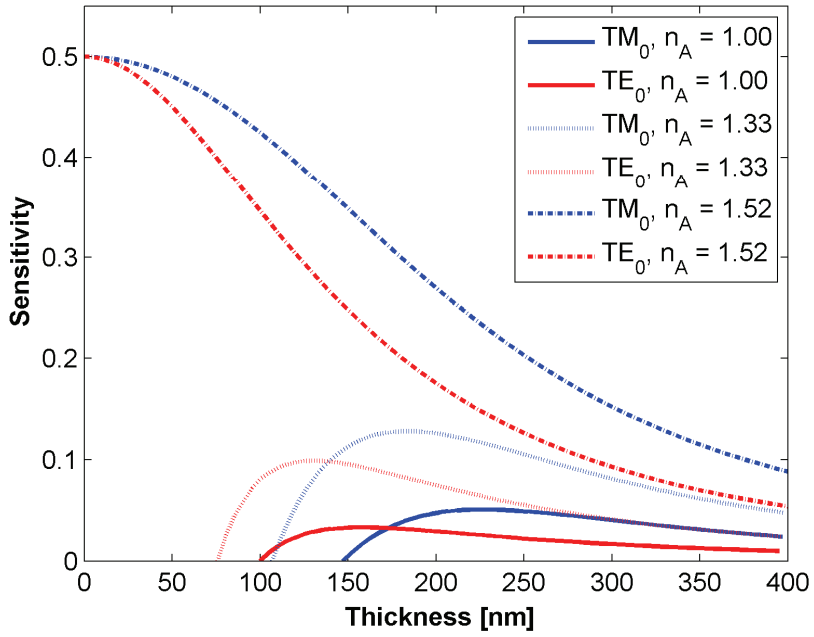

Figure 3.15: Sensitivity of waveguide in cases of three different adlayers.
Waveguide parameters: $n_S = 1.52, n_F = 1.77, n_A = 1.0, 1.33$ *and* $1.52, \lambda = 632.8\ nm$.

Knowledge of the above parameters in the preparatory stage of an OWLS experiment is essential. The wavelength of the laser to be used, the range of the expected adlayer refractive index and the desired sensitivity are all important parameters that influence the choice of the waveguide with proper parameters.

4. Materials and Methods

In all of our experiments the light-induced refractive index change of a thin bacteriorhodopsin layer has been investigated. Measurements of the refractive index change were based on the Optical Waveguide Lightmode Spectroscopy and interferometric techniques. The detailed preparation method of the integrated optical Mach-Zehnder interferometer used in some experiments is out of the scope of this work and described elsewhere [*57*].

a) Instrumentation of the OWLS experiments

The basic principles of the OWLS method are described above, in *Section 3.2*. A single-mode waveguide *(Balzers, Switzerland, n_S=1.515, n_F=1.77 @632.8 nm, d≈200 nm)* equipped by a grating coupler *(2400 lines/mm, Λ=416.66 nm)* is placed on an electronically controlled rotational stage *(Ealing Electro Optics)* with a resolution of about 10^{-4} degrees. Due to the small thickness of the guiding layer and the relatively high grating density, only the diffracted beams of order *m=-1* and *m=1* present, and only the zeroth TM and TE guided modes can be excited. Determination of the waveguide parameters was done by the calibration method described earlier, in the presence of air, as adlayer.

Usually, the measuring light coupled into the waveguide was the linearly polarized beam of a He-Ne laser *(Melles Griot, 632,8 nm, 5 mW)* operating in the TEM_{00} transverse mode. Excitation of the differently polarized waveguide modes was done by rotating the polarization plane of the laser. For calibration purposes, the plane of polarization was rotated so that the incident beam consisted a 1:1 ratio of TM (p-polarized) and TE (s-polarized) waves, otherwise, the intensity of the corresponding polarization used in the measurement was maximized.

In the OWLS experiments, the sample was made by layering a drop of purple membrane suspension on top of the waveguide, above the grating, where the effective incoupling occurs. After drying, the drop formed a thin, homogeneous film containing the protein to be investigated *[Figure 4.1]*.

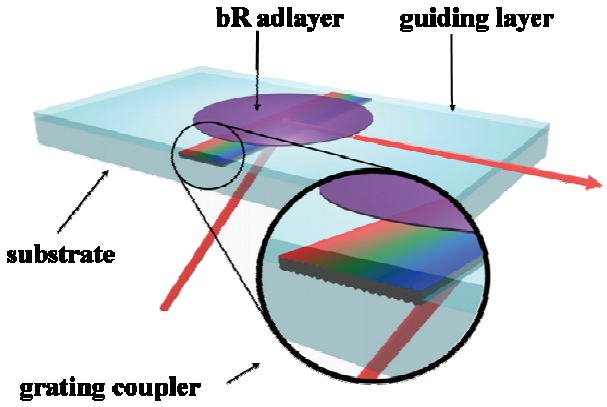

Figure 4.1: The waveguide with grating coupler and the bacteriorhodopsin adlayer.

The protein adlayer of NLO properties was excited using different kinds of lasers, depending on the desired wavelength. Flash excitation of the BR ground state with an absorption maximum at 568 nm was done by the 5 ns pulse of a frequency-doubled Nd:YAG laser *(Continuum, Inc., Surelite-II 10)* operating at 532 nm. The same laser equipped with an Optical Parametric Oscillator *(Continuum, Inc., Surelite OPO)* could be also used for pulse excitation in the wavelength range of 400-700 nm. In some of the experiments, the continuous wave measuring or excitation beams at the wavelengths 413.1, 568.2, 647.1 and 676.4 nm were provided by a Kr^+ gas laser *(Innova I-301, Coherent Inc.)*.

The outcoupled beam was collected by an optical fiber attached to the end of the waveguide and directed to a fast photodiode *(Thorlabs, DET10A)* or a photomultiplier tube *(Hamamatsu, H-5784)*. The electric signal of the detectors were amplified by a home-made voltage amplifier and recorded by a digital oscilloscope *(LeCroy, WaveRunner 6100A)*.

In the next chapter, a brief description concerning the details of each experimental setup will be given.

5. Results and Discussion

Waveguide-based light modulation utilizes the angular shift of the incoupling peaks accompanying the refractive index change due to excitation of the adlayer. Since the guided modes have a significant evanescent component, coupling to or from an external beam is strongly influenced by the refractive index of the material above the grating area. Thus, the change in the refractive index of the adlayer will modulate the incoupling angle. Schematic interpretation of the measurement method is shown in *Figure 5.1* and discussed below.

The angular position of effective incoupling depends on the refractive index of the adlayer. A change of Δn_A in the refractive index causes a corresponding $\Delta\alpha$ shift in the incoupling angle. As it was already shown *[Figure 2.5]*, if there is no change in other parameters of the waveguide, decrease of n_A implies lower effective mode index, consequently, lower (less positive) incoupling angle.

Assume, that the angle of incidence of the beam is fixed at a given value (e.g. α_1). Without excitation, the outcoupled intensity measured at the end of the waveguide is determined by the position of the peak corresponding to the unexcited sample (BR state, blue curve in *Fig. 5.1*). As the refractive index of the adlayer decreases, the peak is shifted to smaller angles (green curve, *Fig. 5.*1) and the intensity measured at the fixed α_1 angle increases. For similar reasons, if the angle of incidence is fixed at a value greater than the center of the initial peak, upon excitation, an intensity decrease can be observed. For a given refractive index change and the corresponding $\Delta\alpha$, the angular dependence of the intensity change around the effective coupling is indicated by the red curve.

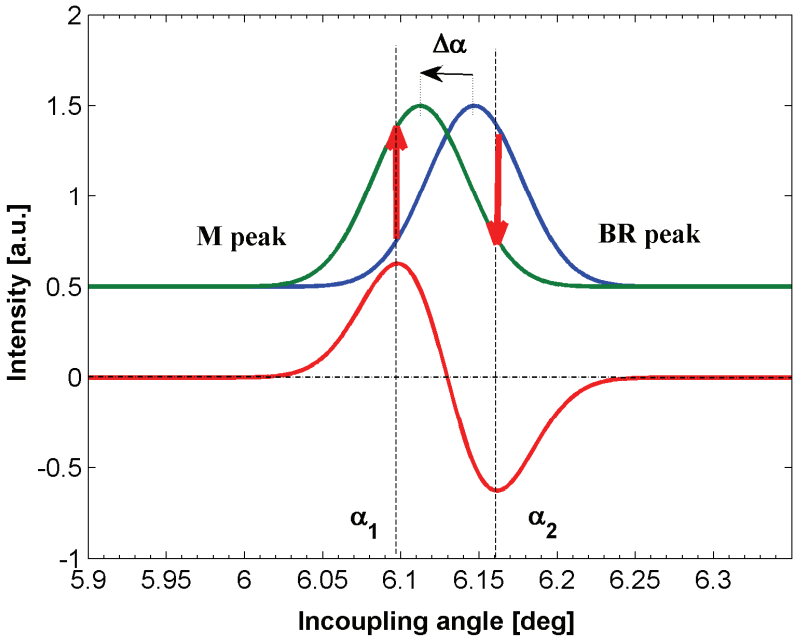

Figure 5.1: Interpretation of the intensity change of the TE mode following refractive index change of the adlayer.

Parameters: $n_S = 1.515, n_F = 1.77, n_{BR} = 1.52, n_M = 1.517, d = 200\ nm, \lambda = 632.8\ nm$,

5.1. Light-driven light-switch based on the photoreactions of the BR and M states

To investigate the refractive index change between the BR and M states, the standard OWLS setup described in *Section 3.2.2.* was used. The light-induced refractive index change of a bR-containing film was demonstrated earlier [*6,58*], although not kinetically resolved. Furthermore, those experiments revealed that under continuous illumination the refractive index changes are consistent with the buildup of the M intermediate state. In order to prove this hypothesis, we performed kinetical experiments.

First, from the angular shift of the incoupling peaks (compared to the case when no bR adlayer is present) the refractive index of the unexcited bR layer was determined to be 1.52, in good agreement of previous findings achieved by using other methods [*6,58*].

In the kinetic experiment, the angle of incidence of the plane polarized measuring beam (He-Ne laser, 5 mW, λ=632.8 nm) was set to different values in the region of effective coupling. We measured the intensity changes of the guided light during the photocycle initiated by an exciting pulse from a Nd:YAG laser (10 mJ pulse energy, λ=532 nm). In order to avoid pre-excitation of the sample, the power of the measuring He-Ne beam was attenuated to 0.5 mW.

Figure 5.2 shows two of the measured intensity changes as functions of time, recorded at opposite sides of the incoupling peak corresponding to the TE mode. The relative change of the light intensity was about 70%.

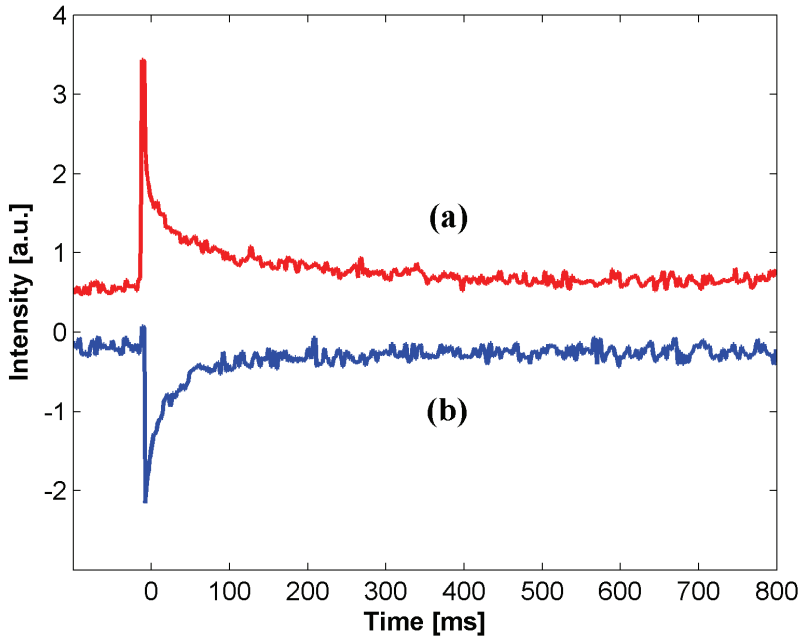

Figure 5.2: Coupled light intensity changes upon flash excitation, measured at the a) left and b) right side of the TE peak.

The traces were analyzed by global fitting with multiexponential curves. In the millisecond region, two exponentials resulted in a good fit, with time constants τ_1=57 ms and τ_2=350 ms, characteristic of the M decay of the photocycle at low humidity [*59*]. From the maximal value of the angular shift, the corresponding refractive index change of the bR adlayer was found to be 2×10^{-3}. This value is close to previous findings [*6,60*]. To correlate the intensity change of the incoupled light with the steps of the photocycle, absorption kinetic measurements were also performed on the same sample, under identical environmental

conditions. The time course of the concentration of the M state was followed by concurrent measurement of the absorption changes at 405 nm upon flash excitation. The obtained time constants were the same as mentioned above, which indicates the Kramers-Kronig origin of the observed refractive index changes corresponding to the large (about 160 nm) difference in the absorption maxima of the BR and M states.

The speed of light modulation based on this effect is therefore limited by the formation of the M intermediate to about 50 μs in the case of WT-bR, using flash excitation. Under continuous illumination, the buildup of the M population (τ_M) and the refractive index changes are limited by the exciting intensity and the decay rate of M, typically to the *ms* time regime.

A faster switch can be devised by making use of the back-photoreaction of the M state. It is well known that blue light shortcuts the photocycle, driving the M form back to the ground state [*36*]. Optical changes accompanied by this photoreaction should be faster than a microsecond. In this experiment, the measuring beam of the He-Ne laser was unattenuated and provided also a continuous exciting illumination. In this case the time constant of accumulation of the M state was about τ_M=15 ms (data not shown). *Figure 5.3* shows the intensity change of the incoupled light measured after a blue flash (Nd:YAG pumped OPO, λ=410 nm) superimposed on the red background illumination.

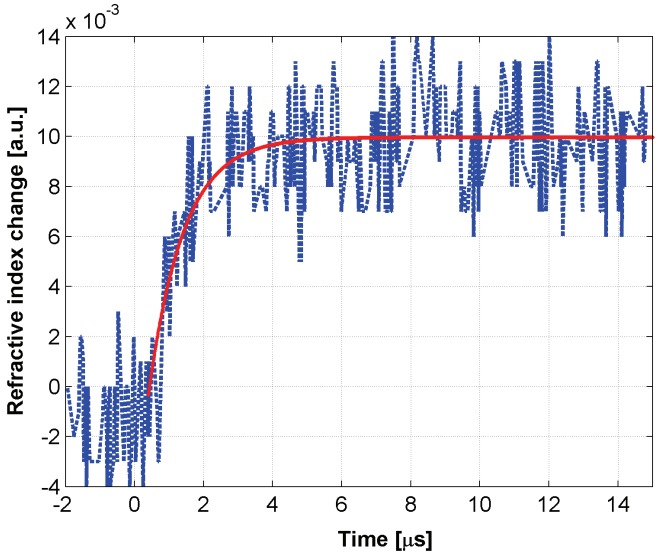

Figure 5.3: Intensity change of the coupled light due to the refractive index change accompanying the flash induced M→BR photoreaction.

The speed of optical switching is characterized by a submicrosecond rate constant (0.8 μs, instrument limited), while the corresponding refractive index change is almost the same as that associated with the BR→M forward reaction, but with opposite sign (1.8×10^{-3}).

Utilizing the tools of OWLS-technique and exploiting the refractive index changes accompanying the BR→M and M→BR photoreactions of a dry bacteriorhodopsin film, all-optical switching on the μs time scale with a modulation efficiency of about 70% was demonstrated. The light-induced refractive index change was found to be about 2×10^{-3}, which is comparable to, and even higher than that of the organic or inorganic crystals used as NLO materials in integrated optics. The above results demonstrate the feasibility of using a protein as a programmable active element in integrated optical devices.

5.2. Integrated optical interferometric light modulation

Previously, a novel method for all-optical light modulation based on the BR→M transition of bacteriorhodopsin [*61*] was introduced. The speed of optical switching, however, was limited by the buildup time of the M state, $\tau_M \approx 50\ \mu s$ in the case of flash-excitation and even slower when the sample is excited by continuous light. The regeneration of the switch was limited by the decay rate of M, typically in the *ms* range, while the modulation efficiency was also limited by the resolution of the OWLS technique. As a next step, we applied another integrated optical structure, and checked the feasibility of light modulation based on a faster transition of the bR photocycle, as well.

The interferometric light modulator was based on an integrated optical Mach-Zehnder interferometer which serves as the passive waveguiding element, while the active role was played by the bacteriorhodopsin-containing purple membrane layer covering the arms of the interferometer. The physical dimensions of the structure allowed direct end-coupling of a laser beam from a single-mode optical fiber with a core diameter of 5 μm. The fiber was placed and fixed close to the end stripes of the interferometer, and finally all the parts were attached to a microscope slide what was used as a substrate to hold the structure. This device formed the basis of the interferometric all-optical switch.

The I_0 intensity of the incoupled light was split into two parts in the photopolymeric waveguide arms (I_1 and I_2). The output intensity was determined by the interference of the two modes:

$$I_{out} = I_1 + I_2 + 2\sqrt{I_1 I_2}\cos(\Delta\varphi),$$

where $\Delta\varphi$ is the phase difference between the modes propagating in the two arms. Without excitation, the initial phase difference depends on the intrinsic antisymmetry of the device, e.g. on the difference in the length of the active regions and non-uniformity of the arms.

The principle of switching is based on the refractive index change of the bR adlayer on one of the arms of the interferometer. When illuminating only one of the arms, the refractive index change of bR leads to a phase shift in that arm, consequently, the output intensity also changes. Therefore, the interference can be changed from constructive to destructive, or the reverse.

Figure 5.4 demonstrates the efficiency of the interferometer-based optical switching. The measuring beam coupled into the interferometer was that of a diode laser (*λ=676 nm, P=8 mW*), while the bR layer covering one of the arms was excited by a CW Ar^+ laser (*Spectra Physics, Stabilite 2016, λ=488 nm, P=25 mW*). After switching on the exciting light, the steady-state is reached within a few seconds, while the decay reflects the relaxation of the refractive index change of the bR film, after the excitation was switched off.

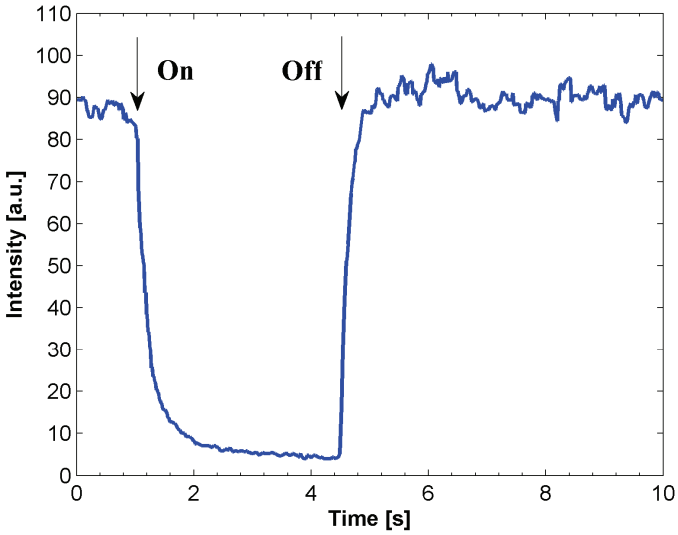

Figure 5.4: Optical switching by the photopolymeric Mach-Zehnder interferometer covered with a bacteriorhodopsin film as adlayer.

The variation of the steady-state intensity measured at the output of the interferometer has been measured also as a function of the exciting power. In the investigated range, two minima and two maxima were observed, however, no saturation of the effect was found despite the relatively high excitation intensity *[Figure 5.5]*.

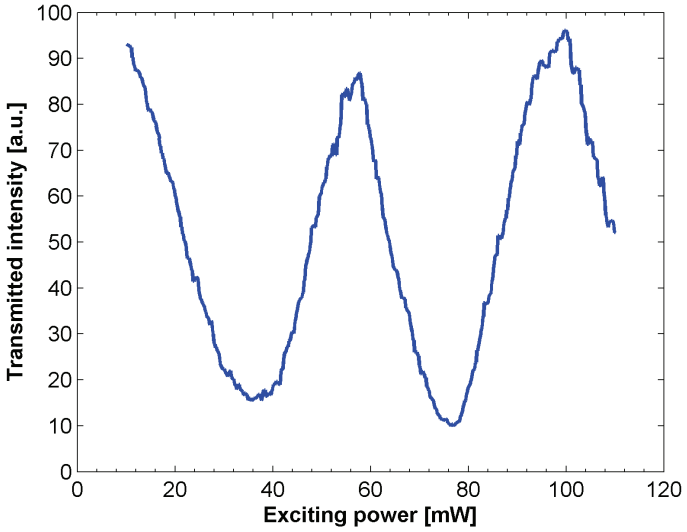

Figure 5.5: Sinusoidal modulation of the transmitted light as a function of exciting power.

Detailed analysis of absorption measurements performed under the same conditions (data not shown) proved that the refractive index change of the sample is originating from the competition between the K and M intermediates. The M intermediate is blue-shifted, while K is red-shifted with respect to the ground state, consequently, their contributions to the refractive index change are of opposite sign. In case of high enough excitation intensity, the contribution of the K intermediate dominates the absorption change, therefore, the refractive index change must be positive, and was estimated to be 9×10^{-4}. This high value which is comparable with that accompanying the BR→M transition but with opposite sign, is interpreted by the anomalous dispersion of K having an absorption maximum close to the wavelength of the measuring light. These results imply that the K intermediate has even more favorable nonlinear optical properties than those of M due to the potentially faster *(ps)* kinetics of its refractive index change and may readily be utilized in integrated optics.

The above results have shown that an effective all-optical switching can be realized even with the fraction of the refractive index change mentioned before [*62*]. Recently,

efficient integrated optical switching with a speed of a few microseconds, based on the M intermediate, has been experimentally demonstrated also at one of the telecommunication wavelengths (1550 nm) [*63,64*].

In the following, we present data supporting the possibility of optical switching based on a six orders of magnitude faster (*ps*) photoreaction of bacteriorhodopsin, involving the K intermediate.

In order to calibrate refractive index changes accompanying the BR→K transition, kinetic experiments were carried out using the grating-coupled planar waveguide. The measuring beam was that of a CW Kr^+ laser (λ=676 nm, P=20 mW), while the excitation have been provided by a Nd:YAG laser ($\tau = 5\ ns$, $\lambda = 532\ nm$, $E_{pulse} = 300\ mJ$). The intensity of the exciting pulse was attenuated in order not to destroy the sample. The angle of incidence was tuned to the coupling of the TE mode and measurements were performed on both sides of the peak.

The measured intensity changes also contain some contribution from absorption changes observed by the measuring light. However, due to symmetry reasons, the contributions originating from absorption and refractive index changes can be easily separated. Since, to a first approximation, the absorption of the bR film is independent of the incident angle, the difference of two individual traces *[Figure 5.6a]* measured on the opposite sides of the peak represent the kinetics of the angular shift (i.e. the kinetics of the refractive index change during the photocycle), while the sum of the traces *[Figure 5.6b]* contains contributions only from absorption.

In order to interpret the above results, one has to consider the photocycle at moderate hydrations, where the N and O intermediates, associated with the proton release and uptake processes under natural conditions, are missing. In this case, contrary to the hydrated samples, the population of the K intermediate remains substantial throughout the whole photocycle, due to the increased rate constants of the M→L and L→K back-reactions [*35*]. Since the rise time of M is in the 10 μs range, the first data points collected after excitation are characteristic to the BR→K transition.

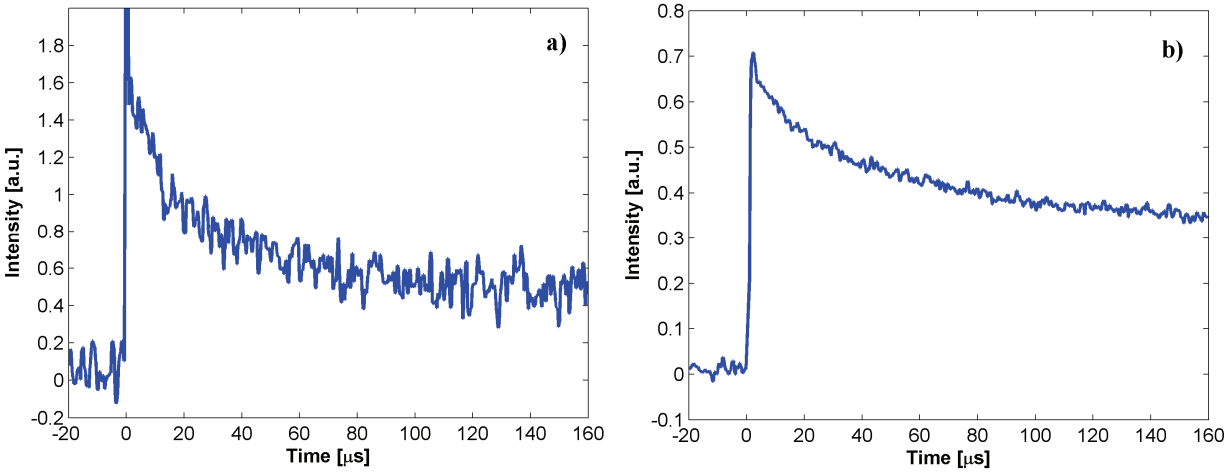

Figure 5.6: a) Difference of traces measured on the two sides of the incoupling peak, representing the kinetics of the refractive index change in the film. b) Sum of the same traces, representing the kinetics of the absorption change in the film.

A global exponential fit to the absorption kinetic and refractive index changes revealed two exponential components ($\tau_1 = 17.8\ \mu s$ and $\tau_2 = 472\ \mu s$) with different weights in the two types of the signals. Based on the above considerations, the faster signal can be assigned to the decay of K to the K-L-M equilibrium, while the slower one corresponds to the subsequent decay of the K-L-M mixture. Considering the absorption spectra of the intermediate states *[Figure 1.5]*, the relative populations of the K and L+M (0.82 and 0.18, respectively) could be determined from the absorption kinetic curves. Using these values as weights in the refractive index difference curves *[Figure 1.6]*, a ratio of refractive index changes associated to the BR→K transition can be deduced.

Calculating with the presence of 15% L intermediate [*65*] in the K-L-M mixture, and with $\Delta n_L / \Delta n_M = 0.3$, we get $\Delta n_K / \Delta n_M = 0.25 \pm 0.05$, which is consistent with the values obtained from the Kramers-Kronig relations. Taking into account our earlier results [*61*], the refractive index change in the BR film accompanied with the BR→K transition at 676 nm is approximately 1×10^{-3}. According to our former experiments using the BR→M molecular transition [*61,62*], this value is high enough to serve as a basis of all-optical switching with a proper integrated optical device.

Further experiments were performed using the Mach-Zehnder interferometer to show that fast integrated optical switching can be achieved based on the BR→K transition of

bacteriorhodopsin. 5 ns long pulses from the Nd:YAG-pumped OPO were coupled into the interferometer coated with bR film on both branches. The wavelength was tuned to the isosbestic point of the BR and K spectra (λ=591 nm, see *Figure 1.5*). Simultaneous pulses from the same Nd:YAG laser (λ=532 nm) were used to excite the bR film asymmetrically, on one arm of the interferometer, only. Under such conditions, a BR-K mixture is developing rapidly, without the accumulation of the later intermediates (L and M), that appear on the microsecond time scale. Hence, intensity changes of the guided light measured at the output can be attributed to refractive index changes of the adlayer, especially due to the BR→K transition *[Figure 5.7]*. The effect was optimized by fine-tuning the initial phase difference of the interferometer using a preillumination of the adlayer above the unexcited arm [*57*].

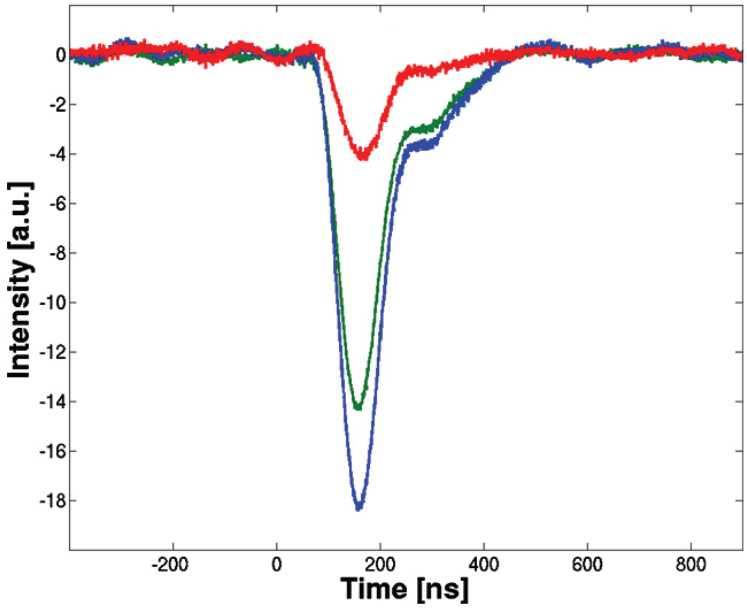

Figure 5.7: Intensity changes of the guided nanosecond pulses (λ=591 nm) with (green) and without (blue) simultaneous excitation (λ=532 nm). Difference of the two curves is depicted in red.

The rise and decay time of the curves is limited by the response time of our photomultiplier and amplifier, but reflect much faster (nanosecond) optical changes accompanying the formation of the K intermediate.

The above results are the first experimental demonstration of an all-optical intensity modulation by bacteriorhodopsin of this speed. The efficiency of the switching can be

improved by optimizing the structure of the interferometer. Taking into account that the rise time of the K intermediate state upon excitation by a femtosecond pulse is in the picosecond range, the above results imply the feasibility of a protein-based ultrafast integrated optical switch, whose application could be advantageous, especially in telecommunication.

5.3. Photonic frequency and amplitude switch

The continuous growth of internet traffic is expected to last for the foreseeable future. The concept of Tbit/s telecommunication represents the expectations of a serious improvement both in capacity and speed and all-optical (photonic) data processing is considered to be the most promising approach to achieve these goals. Here we present the first experimental demonstration of a picosecond photonic switch using the refractive index change of the bR adlayer accompanying the ultrafast BR→K transition, allowing greater than 100 GHz communication speed in integrated optical devices [*66*].

Our first experiments concerning the integrated optical applications of bR proved that under CW illumination, the refractive index of a dried bR-film at 630 nm changes while the M state develops. Consequently, if a probe laser beam at a wavelength outside of the excitation range of bR is coupled into an integrated optical device (e.g. a slab waveguide or a Mach-Zehnder interferometer) covered by an adlayer prepared of bR, the intensity of the output can be modulated by exciting the sample [*61,62*]. Optical switching and logical operations based on the BR→M transition were also shown later by other integrated optical structures, as well [*63,67,68*]. The results of our later experiments (see previous chapter) proved that the BR→K transition can also be utilized in integrated optical applications, suggesting the feasibility of picosecond optical switching, based on the nonlinear optical properties of bacteriorhodopsin.

In order to realize such an ultrafast photonic switching, pump-probe experiments were carried out on a bR film, using picosecond and femtosecond laser pulses. The concept of the measurement was the following: A short pump pulse at a wavelength in the absorption band of bR *(λ=530 nm)* initiated the photocycle of the protein. The light-induced refractive index change was then probed by a subsequent laser pulse at a central wavelength around 790 nm,

outside the absorption bands of all intermediates, ensuring that the photocycle is unaffected by the probe beam. The investigated transition was characterized by changing the time delay between the pump and probe pulses, as well as their duration.

In all experiments pulses generated by a TW-class laser system were used, which provided us with two synchronized pulses centered at 530 nm and 790 nm wavelengths, respectively *[Figure 5.8]*. The broadband pulses *(E=80 μJ, λ=530 nm)* were generated from the more intense part of the fundamental beam with the unique combination of non-collinear optical parametric chirped pulse amplification (NOPCPA) and chirp-assisted sum-frequency generation [*69*]. The less intense part of the beam *(E=1 μJ, λ=790 nm)* was used to probe the sample excited by the pump pulse. After an adjustable delay and shaping of their spectral bandwidth the pulses were aimed to the sample, in this case a slab optical waveguide covered by a dried bacteriorhodopsin layer. The outcoupled spectrum and intensity were monitored by a spectrograph *(OceanOptics, HR4000)* and a fast photodiode *(Thorlabs, DET10A)*, respectively. The traces were recorded by a multichannel analyzer *(LeCroy, WaveRunner 6100A)*.

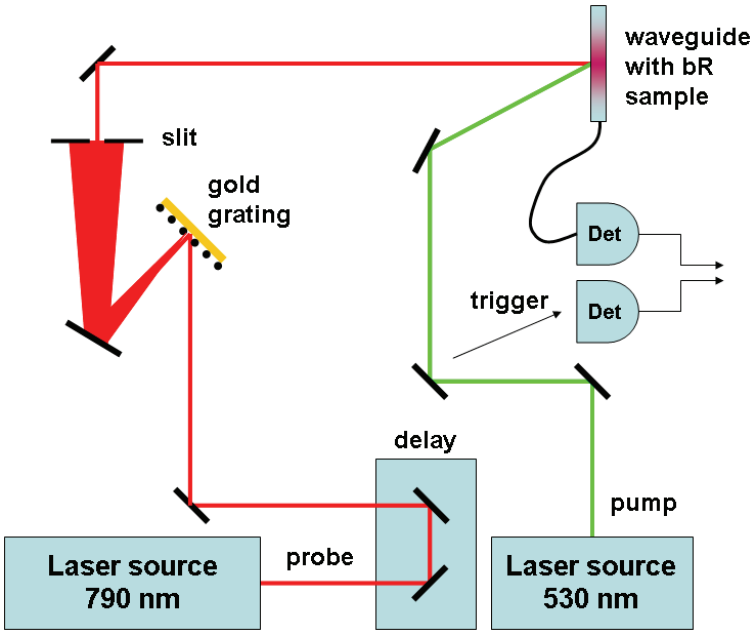

Figure 5.8: Experimental setup of the ps photonic switch.

The duration of the generated pump pulses was 45 ns. The broadband probe pulses were spatially dispersed by a gold reflection grating *(1800 lines/mm)* and a narrow spectral

bandwidth *(between 0.8 nm and 3 nm)* was cut by an optical slit, providing a pulse duration between 3.2 ps and 12 ps.

In all of the measurements the incident angle of the probe pulses was tuned to the incoupling range of the TM peak. Due to the refractive index change of the bR adlayer following excitation, the coupling wavelength of a broadband probe pulse is expected to shift by 0.5-1.0 nm, or, alternatively, the outcoupled intensity of a narrow-band pulse should change. These effects can be detected by a spectrophotometer or by a photodiode, respectively.

5.3.1. The *ps* frequency switch by the BR→K transition

The first series of experiments aimed to demonstrate the frequency shift of the incoupled broadband pulse upon excitation of the bR film. A brief conceptual description of the wavelength shift is the following: The incident angle of the probe beam is fixed at the maximum of the incoupling peak corresponding to the refractive index *(n_A)* of the unexcited sample (BR state), determined by the mode equation. In this way we also fix the effective refractive index of the propagating mode *(N)*. Upon excitation, the refractive index of the adlayer changes. Since no other parameters (e.g. thickness, film refractive index, etc.) of the waveguide have been changed, the wavelength of the propagating wave should change, in order to fulfill the mode equation with the new value of the adlayer refractive index. Therefore, in case of a broadband probe beam, change in the refractive index of the bR adlayer involves a spectral shift of the outcoupled spectrum that can be measured at the end of the waveguide.

During the measurement of the wavelength shift, the FWHM *(full-width-at-half-maximum)* bandwidth of the linearly polarized *(TM, or p-polarized)* probe pulses of 12 ps was chosen to be 3 nm. The spectrum selected by the waveguide was measured by a spectrophotometer. The bR photocycle was initiated by the pump pulse with a duration of 45 ps, reaching the sample 100 ps before the probe. Under these conditions, the only intermediate present in the photocycle is the K form, with a red-shifted absorption spectrum relative to the ground (BR) state. As it was demonstrated earlier, such a spectral shift should result in a refractive index increase of the adlayer, when measured at the wavelength of the

probe pulse. This refractive index change, in turn, involves a red-shift in the incoupled spectrum, provided that the angle of incidence is unchanged. In fact, traces in *[Figure 5.9]* show a red shift in the spectrum of the incoupled light upon excitation.

This type of switching we call "frequency-switching", because one can select different frequency bands of very narrow bandwidth *(<1 nm in this case)* of a broadband pulse, enabling frequency demultiplexing, an essential operation in optical information processing.

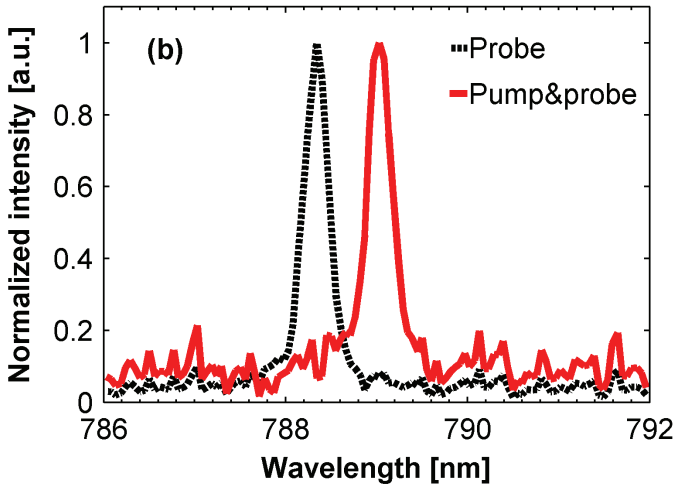

Figure 5.9: The spectral shift of a broadband probe pulse following the excitation of the adlayer.

According to our calculations based on the mode equations [*50,61,70*], the amount of the observed spectral shift corresponds to a refractive index change that is comparable to that observed between BR and M, allowing a direct "amplitude switching".

5.3.2. The *ps* amplitude switch based on the BR→K transition

In the previous section we have seen that in the case of a broadband probe pulse, the refractive index change of the adlayer is followed by a spectral shift of the incoupled spectrum, without any change in the intensity. However, if the spectral shift is larger than, or comparable to the half of the FWHM bandwidth of the probe pulse, a decrease in the intensity can be observed, provided the angle of incidence is set to the maximum of the incoupling

peak. For a quasi-monochromatic, narrow-band probe, an efficient intensity change *(amplitude switching)* is expected, based on the same effect that was described in *Section 5 [Figure 5.1]*.

In order to realize the amplitude switching by the K intermediate, next the bandwidth of the probe pulse was narrowed down to 0.8 nm. The intensity of the outcoupled light was monitored by a fast photodiode. In order to maximize the effect, the angle of incident probe pulse was slightly tuned off the resonance peak, until the output intensity decreased to its half-maximum. As the green pump pulse excites the sample, an angular shift of the incoupling peak occurs and the intensity of the incoupled light increases *[Figure 5.10]*.

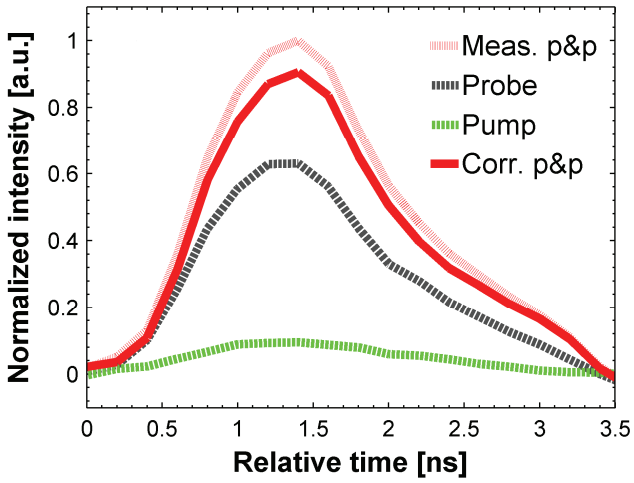

Figure 5.10: The ps amplitude switching.

When both the measuring (probe) and exciting (pump) pulses hit the sample (light red line), the incoupled intensity is considerably higher than that when only the probe beam is present (grey dashed line). A small amount of the exciting light is also reached the detector, when the pump beam was on (green line). Correcting to this, the fast intensity modulation achieved in this experiment was about 50%.

The above results clearly demonstrate the feasibility of ultrafast all-optical frequency and amplitude switching using the picosecond BR→K transition of the bacteriorhodopsin photocycle. More effective switching is expected to be achieved in the future by proper modification of the protein sample [*71*] and optimizing the underlying photonic structure.

6. Conclusions

Integrated optics is a new, rapidly emerging discipline of optical engineering, aiming at the miniaturization and integration of optical elements on a common substrate, analogously to integrated electronics. Contrary to the electronic conductors and transistors, their optical counterparts, waveguides and optical switches serve as passive and active optical information processing elements, respectively. The basic problem of integrated optics is to find proper nonlinear optical materials that can actively control optical circuits. Several materials have been considered for this application requiring high speed and sensitivity, however, so far none of them is regarded as the optimal solution. Besides inorganic and organic crystals, biological molecules have also been considered to be used as active NLO materials, among which the chromoprotein bacteriorhodopsin has generated the most interest.

In this work, integrated all-optical switching based on the nonlinear optical properties of bacteriorhodopsin was investigated. The refractive index of a dried bacteriorhodopsin layer measured at 632 nm was determined using the OWLS technique. The results are consistent with our calculations based on the Kramers-Kronig relations and with experimental results obtained by other methods. Using a grating-coupled slab optical waveguide coated with a thin bR film, effective all-optical switching based on the light-induced refractive index change accompanying the BR→M transition of the photocycle on the microsecond time scale was demonstrated.

Theoretical predictions suggest that the amount of the refractive index change accompanying the BR→K transition should also be enough for optical switching. To check this hypothesis, experiments using a bR-coated integrated Mach-Zehnder interferometer were carried out. Exciting the protein-coating with a CW Ar^+ laser beam *(λ=488 nm)* of increasing power, the output intensity of the incoupled beam of a CW Kr^+ laser *(λ=676 nm)* could be sinusoidally modulated. In this case, refractive index changes during the photocycle were shown to be associated with a kinetic competition between the K and M intermediates. Interferometric pump and probe experiments using measuring and excitation pulses with the duration of several nanoseconds were also performed, to demonstrate fast all-optical switching. In case of such a short excitation, a dynamic equilibrium between the

concentrations of BR and K states is developing, without the accumulation of later (L and M) intermediates. Therefore, the observed refractive index change can be assigned to the BR→K transition, alone. The results imply that the K form has even more favorable nonlinear optical properties than those of M due to its *ps* kinetics of refractive index change.

Experimental realization of ultrafast all-optical amplitude and frequency switching based on the BR→K transition has also been demonstrated. If the duration of the exciting and measuring pulses is in the order of tens of picoseconds, the dominant intermediate state in the sample is the K form. Thus, any observable refractive index change in the sample can be associated to the BR→K transition.

Frequency switching was obtained by using short pump pulses *(τ_{pump}=45 ps, λ_0=530 nm)*, preceding the "broadband" probe beam *(τ_{probe}=12 ps, λ_0=790 nm, $\Delta\lambda$=3 nm)* by 100 ps. Upon excitation, a spectral shift in the outcoupled light can be observed if the bandwidth of the probe is so wide, that the angular range of effective incoupling is larger than the light-induced angular shift. The outcoupled spectrum becomes red-shifted with increasing adlayer refractive index, indicating that the altered propagation conditions are valid for a longer wavelength. The light-induced spectral shift of the outcoupled light can be utilized, for example, in photonic frequency demultiplexers.

In case of a narrow-band probe pulse, the angular shift of the incoupling peak following a light-induced refractive index change of the adlayer involves an intensity change of the outcoupled light. Since the buildup of the K form and, consequently, the associated refractive index change takes place on the *ps* time scale, the effect can be utilized as an ultrafast all-optical amplitude-switch.

The above results show, that bacteriorhodopsin can easily find applications in waveguide-based integrated optical devices, as an active nonlinear optical material. The amount and speed of refractive index changes accompanying the photocycle are comparable to, or even higher than those of the inorganic crystals recently used. Its stability, fast, light-induced, genetically tailorable photochemical reactions and favorable nonlinear optical properties make it a promising candidate in future integrated optical devices. The efficiency of switching can be enhanced further by optimizing the underlying integrated optical structures.

ACKNOWLEDGEMENTS

Though my name is printed on the cover of this thesis, I must pay tribute to the myriad contributions of my advisors and collaborators and the support of my family and friends.

Fist and foremost, I would like to thank my supervisor, Prof. András Dér, Deputy Director of Institute of Biophysics. He has taught me how good experimental physics is done. The technical skills I have learnt from him made it possible for me to implement this thesis. I appreciate all his contributions of time, ideas, and funding to make my Ph.D. experience productive and stimulating. The enthusiasm he has for his research was contagious and motivational for me, even during tough times. I am also thankful for the excellent example he has provided as a successful physicist and professor.

I gratefully acknowledge the continuous support and constructive criticism of Prof. Pál Ormos, Director of Institute of Biophysics and General Director of the Biological Research Centre. His dedication, encouragement and hard work inspired me to better myself and aim higher.

I would also like to express my thanks to the experts of the TeWaTi research group at the University of Szeged, Department of Optics and Quantum Electronics; the *ps* switching experiments would not have been done without their theoretical expertise and technical experience.

Many thanks for my friends, former and present colleagues at the Institute of Biophysics, I could not do the things I have done without your help, loyalty and friendship. I hesitate to include such a list, as I surely omit some who deserve mention.

Finally, I would like to dedicate this work to my family for all their love and encouragement. Without your unending support from childhood to now, I never would have made it through this process or any of the tough times in my life. Thank you.

László Fábián

Institute of Biophysics

June 2012

Bibliography

1. G. E. Moore, Electronics **38** (1965).

2. S. A. Haque and J. Nelson, Science **327**, 1466 (2010).

3. X. Hu, P. Jiang, C. Ding *et al*, Nat. Phot. **2**, 185 (2008).

4. J. M. Hales, J. Matichak, S. Barlow *et al*, Science **327**, 1485 (2010).

5. N. Vsevolodov, *Biomolecular electronics*. (Birkhauser, Boston, 1998).

6. D. Zeisel and N. Hampp, J. Phys. Chem. **96**, 7788 (1992).

7. J. A. Stuart, D. L. Marcy and R. R. Birge, in *Bioelectronic Applications of Photochromic Pigments*, edited by A. Dér and L. Keszthelyi (2001), pp. 15.

8. E. Korchemskaya, N. Burykin, S. Bugaychuk *et al*, Photochem. Photobiol. **83**, 403 (2007).

9. D. Oesterhelt and W. Stoeckenius, Nature New Biology **233**, 149 (1971).

10. D. Oesterhelt and W. Stoeckenius, PNAS **70**, 2853 (1973).

11. D. Oesterhelt and W. Stoeckenius, in *Meth. Enzymol.*, edited by S. Fleischer and L. Packer (Academic Press, 1974), Vol. 31, pp. 667.

12. W. Stoeckenius, R. H. Lozier and R. A. Bogomolni, Biochim. Biophys. Acta **505** (3–4), 215 (1979).

13. A. Dér, R. Tóth-Boconádi, L. Keszthelyi *et al*, FEBS Lett. **377** (3), 419 (1995).

14. W. Stoeckenius, Trends Biochem. Sci. **10** (12), 483 (1985).

15. R. A. Bogomolni, R. H. Lozier and W. Stoeckenius, Biophys. J. **16** (2), A21 (1976).

16. W. Stoeckenius, Bioelectrochem. Bioenerg. **3** (3-4), 371 (1976).

17. J. W. Belliveau and J. K. Lanyi, Arch. Biochem. Biophys. **178** (1), 308 (1977).

18. R. Hartmann, H.-D. Sickinger and D. Oesterhelt, FEBS Lett. **82**, 1 (1977).

19. R. Henderson and D. Shotton, J. Mol. Biol. **139** (2), 99 (1980).

20. R. Henderson, J. M. Baldwin, K. H. Downing *et al*, Ultramicroscopy **19** (2), 147 (1986).

21. R. Henderson, J. M. Baldwin, R. A. Ceska *et al*, Cell Biol. Int. Rep. **14, Supplement 1** (0), 25 (1990).

22. Yu A. Ovchinnikov, N. G. Abdulaev, M. Yu Feigina *et al*, FEBS Lett. **100** (2), 219 (1979).

23. H. Luecke, B. Schobert, H. T. Richter *et al*, J. Mol. Biol. **291**, 899 (1999).

24. U. Fischer and D. Oesterhelt, Biophys. J. **28** (2), 211 (1979).

25. W. Sperling, C. N. Rafferty, K.-D. Kohl *et al*, FEBS Lett. **97** (1), 129 (1979).

26. R. Casadio, H. Gutowitz, P. Mowery *et al*, Biochim. Biophys. Acta **590** (1), 13 (1980).

27. T. Kouyama, R. A. Bogomolni and W. Stoeckenius, Biophys. J. **48** (2), 201 (1985).

28. M. Chu Kung, D. DeVault, B. Hess *et al*, Biophys. J. **15** (9), 907 (1975).

29. R. H. Lozier, R. A. Bogomolni and W. Stoeckenius, Biophys. J. **15** (9), 955 (1975).

30. A. Dér, S. Száraz, R. Tóth-Boconádi *et al*, PNAS **88**, 4751 (1991).

31. K. J. Kaufmann, P. M. Rentzepis, W. Stoeckenius *et al*, Biochem. Biophys. Res. Comm. **68** (4), 1109 (1976).

32. R. H. Lozier, W. Niederberger, R. A. Bogomolni *et al*, Biochim. Biophys. Acta **440** (3), 545 (1976).

33. W. V. Sherman, M. A. Slifkin and S. R. Caplan, Biochim. Biophys. Acta **423** (2), 238 (1976).

34. G. Váró and J. K. Lanyi, Biophys. J. **56** (6), 1143 (1989).

35. G. Váró and J. K. Lanyi, Biophys. J. **59** (2), 313 (1991).

36. P. Ormos, Z. Dancsházy and L. Keszthelyi, Biophys. J. **31**, 207 (1980).

37. S. P. Balashov, Isr. J. Chem. **35**, 415 (1995).

38. J. P. Cartailler and H. Luecke, Annu. Rev. Biophys. Biomol. Struct. **32**, 285 (2003).

39. M. Engelhard, B. Hess, M. Chance *et al*, FEBS Lett. **222** (2), 275 (1987).

40. M. Kataoka, K. Mihara, H. Kamikubo *et al*, FEBS Lett. **333** (1–2), 111 (1993).

41. M. Walther, B. Fischer, M. Schall *et al*, Chem. Phys. Lett. **332** (3–4), 389 (2000).

42. I. Jones, T. J. Rainsford, B. Fischer *et al*, Vibr. Spect. **41** (2), 144 (2006).

43. A. Barth, Biochim. Biophys. Acta **1767** (9), 1073 (2007).

44. H. Saitô and A. Naito, Biochim. Biophys. Acta **1768** (12), 3145 (2007).

45. G. I. Groma, A. Colonna, J.-L. Martin *et al*, Biophys. J. **100** (6), 1578 (2011).

46. C. Gergely, L. Zimányi and G. Váró, J. Phys. Chem. B **101** (45), 9390 (1997).

47. L. Zimányi, J. Phys. Chem. B **108**, 4199 (2004).

48. H. M. Nussenzveig, *Casuality and Dispersion Relations*. (Academic Press, New York, 1972).

49. F. Wooten, *Optical Properties of Solids*. (Academic Press, New York, 1972).

50. K. Tiefenthaler and W. Lukosz, JOSA B Opt. Phys. **6**, 209 (1989).

51. K. Tiefenthaler and W. Lukosz, Thin Solid Films **126** (3–4), 205 (1985).

52. Ph M. Nellen, K. Tiefenthaler and W. Lukosz, Sensors and Actuators **15** (3), 285 (1988).

53. K. Tiefenthaler, Biosens. Bioelec. **8** (7–8), xxxv (1993).

54. R. E. Kunz, Sens. Actuators B **38** (1–3), 13 (1997).

55. M. Wiki, R. E. Kunz, G. Voirin *et al*, Biosens. Bioelec. **13** (11), 1181 (1998).

56. J. Vörös, J. J. Ramsden, G. Csúcs *et al*, Biomaterials **23**, 3699 (2002).

57. A. Dér, S. Valkai, A. Mathesz *et al*, Sens. Actuators B **151** (1), 26 (2010).

58. C. P. Zhang, C. Y. Ku, Q. W. Song *et al*, Opt. Lett. **19**, 1409 (1994).

59. G. Váró, in *Conference Proceedings of the Bioelectronic Applications of Photochromic Pigments, Szeged, Hungary, 2000*, edited by A. Dér and L. Keszthelyi (IOS Press, Amsterdam, 2001), p. 149.

60. Q. W. Song, C. P. Zhang, R. B. Gross *et al*, Opt. Lett. **18**, 775 (1993).

61. P. Ormos, L. Fábián, L. Oroszi *et al*, Appl. Phys. Lett. **80**, 4060 (2002).

62. A. Dér, S. Valkai, L. Fábián *et al*, Photochem. Photobiol. **83**, 393 (2007).

63. J. Topolancik and F. Vollmer, Appl. Phys. Lett. **89**, 184103 (2006).

64. J. Topolancik and F. Vollmer, Biophys. J. **92**, 2223 (2007).

65. Z. Batori-Tartsi, K. Ludmann and G. Váró, J. Photochem. Photobiol. B **49** (2–3), 192 (1999).

66. L. Fábián, Z. Heiner, M. Mero *et al*, Opt. Expr. **19**, 18861 (2011).

67. S. Roy, M. Prasad, J. Topolancik *et al*, J. Appl. Phys. **107**, 053115 (2010).

68. E. K. Wolff and A. Dér, Nanotech. Perceptions **6**, 51 (2010).

69. M. Mero, A. Sipos, G. Kurdi *et al*, Opt. Expr. **19**, 9646 (2011).

70. J. Vörös, J. J. Ramsden, G. Csúcs *et al*, Biomaterials **23** (17), 3699 (2002).

71. A. Aharoni, B. Hou, N. Friedman *et al*, Biochemistry-Moscow **66**, 1210 (2001).